

.....

Department of Aerospace Engineering, Ryerson University, Toronto, ON M5B 2K3, Canada
e-mail: jenright@ryerson.ca

In this paper, we present a novel approach to planetary rover localization that incorporates sun sensor and inclinometer data directly into a stereo visual odometry pipeline. Utilizing the absolute orientation information provided by the sun sensor and inclinometer significantly reduces the error growth of the visual odometry path estimate. The measurements have very low computation, power, and mass requirements, providing localization improvement at nearly negligible cost. We describe the mathematical formulation of error terms for the stereo camera, sun sensor, and inclinometer measurements, as well as the bundle adjustment framework for determining the maximum likelihood vehicle transformation. Extensive results are presented from experimental trials utilizing data collected during a 10-km traversal of a Mars analogue site on Devon Island in the Canadian high Arctic. We also illustrate how our approach can be used to reduce the computational burden of visual odometry for planetary exploration missions. © 2012 Wiley Periodicals, Inc.

The paper is organized as follows. In Section 2, we examine relevant prior work on visual odometry and review the use of sun sensors in rover navigation. Section 3 outlines the mathematical formulation of our estimation framework. Section 4 provides the details of our experimental test data acquired at a Mars analogue site on Devon Island in the Canadian Arctic (see Figure 1). In Section 5, we present detailed results from the experimental trials. This includes an evaluation of stereo feature detectors, a demonstration of how the sun sensor and inclinometer measurements greatly improve VO estimates, and an examination of the computational gains made possible by this algorithm. The paper concludes with a discussion of our results and proposed future work.



Figure 1. The pushcart rover platform (with support vehicles) on Devon Island, a well-known planetary analogue site in the Canadian high Arctic.

2. PRIOR WORK

The original VO system was introduced by Moravec (1980) in his doctoral thesis. The implementation was simple, but it was the first to contain the basic elements of the modern VO pipeline: a feature detector, a feature matcher, and a motion estimator. This basic model was continued by Matthies, who achieved significantly better accuracy by treating motion estimation as a statistical estimation problem and modeling the feature uncertainties as ellipsoidal three-dimensional Gaussians (Matthies & Shafer, 1987; Matthies, 1992).

The VO system outlined by Matthies formed the basis of the MER algorithm (Matthies et al., 2007), which we will examine in detail now. First, a pair of stereo images are acquired, and features are found in each image using the Harris corner detector (Harris & Stephens, 1988). Features are then matched across the stereo pair using pseudo-normalized cross correlation. After the rover moves a short distance, a second stereo pair are acquired, and features are matched across the two pairs. Next, a random sample consensus (RANSAC) process is performed, which removes outliers and produces a coarse initial motion estimate using a closed-form least-squares calculation. Finally, a maximum likelihood estimate of the motion is iteratively computed, utilizing the three-dimensional covariances of the features (Maimone et al., 2007).

A number of research labs have been investigating variations on and extensions of this basic pipeline. Notable results have been obtained by Konolige, Agrawal, and Solà (2007) at SRI International, who extended the VO algorithm to include incremental sparse bundle adjustment (SBA). Features are detected using an efficient center surround external (CenSurE) interest operator. The estimate errors are minimized by solving a sparse bundle adjustment over a handful of recent frames. Inertial measurement unit (IMU) data are fused with VO estimates using an extended Kalman filter (EKF) to minimize the long term positional drift. Other notable systems have been developed by Mei, Sibley, Cummins, Newman, and Reid (2011), Nister, Naroditsky, and Bergen (2006), and Howard (2008), among others.

The main focus of this paper is on using sun sensor and inclinometer measurements to aid visual odometry motion estimates. The inclusion of a sun sensor on future rover missions was one of the recommendations made after the 1997 Mars Pathfinder mission (Wilcox & Nguyen, 1998). Subsequently, there were several studies at NASA's Jet Propulsion Lab of the use of a dedicated sun sensor for rover navigation. A VO simulation study by Olson et al. (2003) found that long-range position error grows super-linearly with the distance traveled, predominantly because of the contribution of orientation error. However, if absolute orientation measurements are available, the error is bounded to grow linearly with distance. Volpe (1999) performed field tests using the Rocky 7 rover, in which wheel odometry motion estimates were corrected using a sun sensor, in conjunction with an accelerometer to determine sensor tilt. These tests experimentally verified that the use of an absolute orientation sensor can restrict the positional error of a rover to grow linearly. Additionally, Trebi-Ollennu et al. (2001) describe the design and testing of a sun sensor on one of the FIDO rover platforms, reporting errors in rover heading of a few degrees. However, to economize, the MERs were launched without dedicated sun sensors and instead used the PANCAM stereo camera pair to search for and acquire images of the sun (Eisenman et al., 2002). This sun sensing technique is only used as a periodic heading or attitude update, not a direct component of any online navigation algorithm. This sun sensing procedure had only been used about 100 times as of January 2007 (Maimone et al., 2007).

More recently, Furgale, Enright, and Barfoot (2011) presented an experimental study of sun sensing as a rover navigational aid. Navigational information is estimated using sun measurements, a local clock, quasi-analytical models of the solar ephemeris, and, in some cases, a gravity vector measurement from an inclinometer. An estimate utilizing multiple measurements is determined by minimizing a scalar-weighted cost function. With these techniques, the absolute heading of the rover could be determined to within a few degrees. In this paper, these techniques were used to produce periodic attitude updates for

comparison to our technique, in which the sun sensor measurements are used directly in the VO pipeline.

In summary, although significant research has been focused on VO and sun-sensor-aided navigation, the algorithm presented in this paper is the first to incorporate sun sensor measurements directly into the VO formulation. This novel approach provides considerable benefits for planetary rover exploration, as detailed in the following sections. The experiments presented in this paper are based on the work of Lambert, Furgale, Barfoot, and Enright (2011), with the following extensions: (i) an evaluation of popular key point detectors; (ii) an examination of the benefits of using key-point scale information; (iii) uncertainty envelopes for experimental results; (iv) results for a full 10-km traverse; and (v) an experimental demonstration of our technique for reducing the computational cost of VO using sun sensor and inclinometer measurements. Additionally, our implementation has been improved slightly since this previous publication, producing the more accurate and smooth results presented in this paper.

3. MATHEMATICAL FORMULATION

In this section, we outline the mathematical formulation of our VO solution with sun sensor and inclinometer measurements. We start by establishing notational and mathematical conventions and defining our key coordinate frames. We then outline the derivation of the error terms for the stereo camera, sun sensor, and inclinometer. Finally, we discuss the bundle adjustment formulation that allows us to incorporate sun sensor and inclinometer measurements into the estimation solution as they are acquired. This approach enables us to constantly correct the orientation estimate of VO using absolute orientation information, preventing super-linear growth of error.

3.1. Preliminaries

For the sake of clarity, we will briefly outline the notational scheme used in this paper. Vectors are represented by bold face lower case characters, and matrices by bold face upper case characters. The identity matrix is represented by $\mathbf{1}$, whereas a zero matrix is written as $\mathbf{0}$. An overbar denotes the nominal value of a quantity, a circumflex over the top of an element indicates that it is an estimate of a true quantity, and a tilde signifies a measured value. The vector $\rho_a^{D,E}$ represents a translation from point E to point D , expressed in coordinate frame \mathcal{F}_a . The rotation matrix $\mathbf{C}_{a,b}$ rotates vectors expressed in \mathcal{F}_b into \mathcal{F}_a . We use the following set of three standard rotation matrices, using the shorthand $c_\theta := \cos \theta$ and $s_\theta := \sin \theta$:

$$\mathbf{R}_x(\theta) = \begin{bmatrix} 1 & 0 & 0 \\ 0 & c_\theta & s_\theta \\ 0 & -s_\theta & c_\theta \end{bmatrix}, \quad \mathbf{R}_y(\theta) = \begin{bmatrix} c_\theta & 0 & -s_\theta \\ 0 & 1 & 0 \\ s_\theta & 0 & c_\theta \end{bmatrix},$$

$$\mathbf{R}_z(\theta) = \begin{bmatrix} c_\theta & s_\theta & 0 \\ -s_\theta & c_\theta & 0 \\ 0 & 0 & 1 \end{bmatrix}.$$

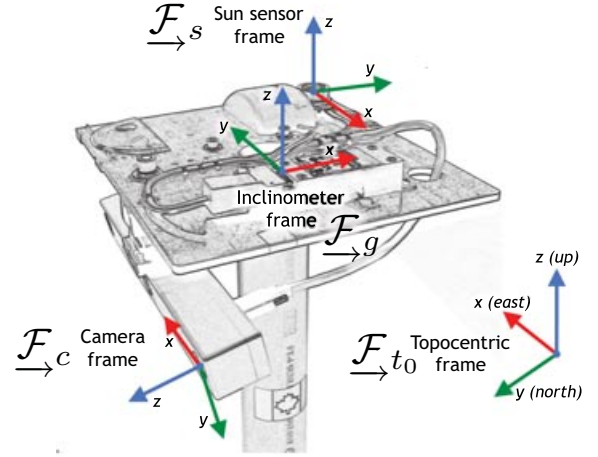


Figure 2. Illustration of the coordinate frames used in our formulation.

Given any 3×1 vector $\mathbf{r} = [r_1 \ r_2 \ r_3]^T$, we can also define the usual 3×3 skew-symmetric cross operator (Hughes, 1986):

$$\mathbf{r}^\times := \begin{bmatrix} 0 & -r_3 & r_2 \\ r_3 & 0 & -r_1 \\ -r_2 & r_1 & 0 \end{bmatrix}.$$

We will now discuss notation for the linearization of rotations, which will be used extensively throughout this paper. Let us define a rotation matrix $\mathbf{C}(\theta)$, where θ is a 3×1 column of Euler angles that define the rotation. A perturbation in this rotation matrix can be written

$$\mathbf{C}(\bar{\theta} + \delta\theta) \approx (\mathbf{1} - (\mathbf{S}(\bar{\theta})\delta\theta)^\times)\mathbf{C}(\bar{\theta}), \quad (1)$$

where $\bar{\theta}$ is the nominal value, $\delta\theta$ is the perturbation, $\mathbf{S}(\bar{\theta})$ is the matrix relating rotation vectors to Euler angles evaluated at the operating point, and $\mathbf{C}(\bar{\theta})$ is the rotation matrix at the operating point. We note that this expression describes how a perturbation of a rotation matrix corresponds to a perturbation of Euler angles, $\bar{\theta} + \delta\theta$. Notationally, it is simpler to write this expression as

$$\mathbf{C}(\bar{\theta} + \delta\theta) = (\mathbf{1} - \delta\phi^\times)\mathbf{C}(\bar{\theta}), \quad (2)$$

where $\delta\phi := \mathbf{S}(\bar{\theta})\delta\theta$ is a 3×1 rotation vector (Hughes, 1986).

3.2. Important Coordinate Frames

Our estimation framework relies on four main coordinate frames, with which we can describe all of our measurements and vehicle transformations. Figure 2 shows the sensor head used in our experiments, with each of the relevant coordinate frames defined.

The camera frame, \mathcal{F}_c , is defined with the origin at the left camera of the stereo apparatus. The x -axis is aligned with horizontal pixels, the y -axis with vertical pixels, and the z -axis with the optical axis. The sun sensor frame, \mathcal{F}_s , is defined having a z -axis aligned with the outward normal of the sensor. For the

inclinometer frame, \mathcal{F}_g , the x - and y -axes of the frame are defined by the orthogonal sensing axes of the sensor. The locally defined topocentric frame, \mathcal{F}_t , is such that the x -axis points in the eastward direction, the y -axis points north, and the z -axis is opposite to the local gravity vector.

With these definitions in hand, we can describe the pose of our rover. The estimate frame in our formulation, \mathcal{F}_{t_0} , has the orientation of the topocentric frame and is located at the origin of our GPS unit at time $t = 0$. At each time step k , we calculate the translation, $\rho_{t_0}^{c_k, t_0}$, and rotation, \mathbf{C}_{c_k, t_0} , of the camera frame \mathcal{F}_c relative to \mathcal{F}_{t_0} , which can easily be transformed to a vehicle frame using calibration information.

3.3. Derivation of Error Terms

Given the stereo camera, sun sensor, and inclinometer measurements recorded at time k , our goal is to determine the maximum-likelihood camera transformation at this time step. Our method is to use a bundle adjustment approach that will estimate the states $\{\mathbf{C}_{c_k, t_0}, \rho_{t_0}^{c_k, t_0}\}$ and $\{\mathbf{C}_{c_{k-1}, t_0}, \rho_{t_0}^{c_{k-1}, t_0}\}$ and the positions of the stereo camera landmarks $\mathbf{p}_{t_0}^{j, t_0}$. Unlike the standard VO approach, which solves for a relative transformation from time $k-1$ to k , we solve for the states relative to \mathcal{F}_{t_0} ; this is because our new sun sensor and inclinometer measurement error terms require a current estimate of the vehicle orientation relative to the topocentric frame. In this technique, Gauss–Newton optimization is used to minimize an objective function composed of Mahalanobis distances proportional to the negative log likelihood of all the measurements. To build this objective function, we require error terms for each of the individual sensors, which we will derive in detail in this section.

3.3.1. Stereo Camera Model

We will now describe the observation models for our sensors, beginning with a stereo camera model. Note that we are not performing multiframe VO in this paper, but instead only matching stereo keypoints frame to frame, as on the MERs. Accordingly, we begin with an initial stereo image pair at time $k-1$, and then a second at time k . Our goal is to determine the translation and rotation of the camera between the two image pairs by estimating the two states, $\{\mathbf{C}_{c_k, t_0}, \rho_{t_0}^{c_k, t_0}\}$ and $\{\mathbf{C}_{c_{k-1}, t_0}, \rho_{t_0}^{c_{k-1}, t_0}\}$. Our measurements are (u_l, v_l) and (u_r, v_r) , the pixel locations of observed keypoints in the left and right rectified stereo images, respectively. The projection of landmark j , with three-dimensional location $\mathbf{p}_{c_k}^{j, c_k} = [x \ y \ z]^T$, into the image plane is described by our observation model for a stereo camera,

$$\mathbf{y}_k^j = \mathbf{h}(\mathbf{p}_{c_k}^{j, c_k}) = \begin{bmatrix} u_l \\ v_l \\ u_r \\ v_r \end{bmatrix} = \frac{1}{z} \begin{bmatrix} f_u(x + \frac{b}{2}) \\ f_v y \\ f_u(x - \frac{b}{2}) \\ f_v y \end{bmatrix} + \begin{bmatrix} c_u \\ c_v \\ c_u \\ c_v \end{bmatrix} + \delta \mathbf{y}_k^j, \quad (3)$$

where f_u and f_v are the horizontal and vertical focal lengths (in pixels), b is the camera baseline, and $\delta \mathbf{y}_k^j$ is the noise associated

with each measurement, modeled as a zero-mean Gaussian density with covariance $\mathbf{T}_{y_k^j}$. Thus, we can define the error term for stereo measurements as follows:

$$\mathbf{e}_{y_k}^j = \mathbf{y}_k^j - \mathbf{h}(\mathbf{p}_{c_k}^{j, c_k}). \quad (4)$$

The three-dimensional location of the landmark relative to the camera frame at time k , $\mathbf{p}_{c_k}^{j, c_k}$, can be expressed as follows:

$$\mathbf{p}_{c_k}^{j, c_k} = \mathbf{C}_{c_k, t_0} (\mathbf{p}_{t_0}^{j, t_0} - \rho_{t_0}^{c_k, t_0}). \quad (5)$$

To linearize the error term (4), we first perturb the feature location (5) about its nominal value, as follows:

$$\begin{aligned} \mathbf{p}_{c_k}^{j, c_k} &= \bar{\mathbf{p}}_{c_k}^{j, c_k} + \delta \mathbf{p}_{c_k}^{j, c_k} \\ &\approx (\mathbf{I} - \delta \Phi_k^\times) \bar{\mathbf{C}}_{c_k, t_0} (\bar{\mathbf{p}}_{t_0}^{j, t_0} + \delta \mathbf{p}_{t_0}^{j, t_0} - \bar{\rho}_{t_0}^{c_k, t_0} - \delta \rho_{t_0}^{c_k, t_0}). \end{aligned}$$

Expanding and eliminating the products of small perturbation terms gives

$$\begin{aligned} \mathbf{p}_{c_k}^{j, c_k} &\approx \bar{\mathbf{C}}_{c_k, t_0} (\bar{\mathbf{p}}_{t_0}^{j, t_0} - \bar{\rho}_{t_0}^{c_k, t_0}) + \bar{\mathbf{C}}_{c_k, t_0} \delta \mathbf{p}_{t_0}^{j, t_0} - \bar{\mathbf{C}}_{c_k, t_0} \delta \rho_{t_0}^{c_k, t_0} \\ &\quad + \delta \Phi_k^\times \bar{\mathbf{C}}_{c_k, t_0} (\bar{\rho}_{t_0}^{c_k, t_0} - \bar{\mathbf{p}}_{t_0}^{j, t_0}). \end{aligned}$$

Using the identity $\mathbf{a}^\times \mathbf{b} \equiv -\mathbf{b}^\times \mathbf{a}$, we can rewrite the perturbed feature position as

$$\begin{aligned} \mathbf{p}_{c_k}^{j, c_k} &= \bar{\mathbf{C}}_{c_k, t_0} (\bar{\mathbf{p}}_{t_0}^{j, t_0} - \bar{\rho}_{t_0}^{c_k, t_0}) + \bar{\mathbf{C}}_{c_k, t_0} \delta \mathbf{p}_{t_0}^{j, t_0} - \bar{\mathbf{C}}_{c_k, t_0} \delta \rho_{t_0}^{c_k, t_0} \\ &\quad + (\bar{\mathbf{C}}_{c_k, t_0} (\bar{\mathbf{p}}_{t_0}^{j, t_0} - \bar{\rho}_{t_0}^{c_k, t_0}))^\times \delta \Phi_k. \end{aligned}$$

This equation can be written in matrix form as

$$\mathbf{p}_{c_k}^{j, c_k} = \bar{\mathbf{p}}_{c_k}^{j, c_k} + [\mathbf{D}_x \ \mathbf{D}_p] \begin{bmatrix} \delta \mathbf{x} \\ \delta \mathbf{p} \end{bmatrix}, \quad (6)$$

where

$$\begin{aligned} \bar{\mathbf{p}}_{c_k}^{j, c_k} &= \bar{\mathbf{C}}_{c_k, t_0} (\bar{\mathbf{p}}_{t_0}^{j, t_0} - \bar{\rho}_{t_0}^{c_k, t_0}), \\ \mathbf{D}_x &= \begin{bmatrix} \mathbf{0} & \mathbf{0} & -\bar{\mathbf{C}}_{c_k, t_0} \end{bmatrix} (\bar{\mathbf{C}}_{c_k, t_0} (\bar{\mathbf{p}}_{t_0}^{j, t_0} - \bar{\rho}_{t_0}^{c_k, t_0}))^\times, \\ \mathbf{D}_p &= \bar{\mathbf{C}}_{c_k, t_0}, \quad \delta \mathbf{x} = \begin{bmatrix} \delta \rho_{t_0}^{c_{k-1}, t_0} \\ \delta \Phi_{k-1} \\ \delta \rho_{t_0}^{c_k, t_0} \\ \delta \Phi_k \end{bmatrix}, \quad \delta \mathbf{p} = \delta \mathbf{p}_{t_0}^{j, t_0}. \end{aligned}$$

Substituting (6) into (4), we obtain our linearized error term,

$$\begin{aligned} \mathbf{e}_{y_k}^j &\approx \mathbf{y}_k^j - \mathbf{h}(\bar{\mathbf{p}}_{c_k}^{j, c_k} + [\mathbf{D}_x \ \mathbf{D}_p] \begin{bmatrix} \delta \mathbf{x} \\ \delta \mathbf{p} \end{bmatrix}) \\ &\approx \mathbf{y}_k^j - \mathbf{h}(\bar{\mathbf{p}}_{c_k}^{j, c_k}) - \frac{\partial \mathbf{h}}{\partial \mathbf{p}} \bigg|_{\bar{\mathbf{p}}_{c_k}^{j, c_k}} [\mathbf{D}_x \ \mathbf{D}_p] \begin{bmatrix} \delta \mathbf{x} \\ \delta \mathbf{p} \end{bmatrix} \\ &= \mathbf{y}_k^j - \mathbf{h}(\bar{\mathbf{p}}_{c_k}^{j, c_k}) - [\mathbf{A}_k^j \ \mathbf{B}_k^j] \begin{bmatrix} \delta \mathbf{x} \\ \delta \mathbf{p} \end{bmatrix}, \quad (7) \end{aligned}$$

where

$$\mathbf{A}_k^j = \mathbf{E}_k \mathbf{D}_x, \quad \mathbf{B}_k^j = \mathbf{E}_k \mathbf{D}_p, \quad \mathbf{E}_k = \frac{\partial \mathbf{h}}{\partial \mathbf{p}} \bigg|_{\mathbf{p}_{c_k}^{j,c_k}}.$$

Following the same logical progression, an analogous error term can be derived for the same landmark observed at time $k - 1$, which will depend on the state perturbation terms, $\delta \mathbf{p}_{t_0}^{c_{k-1}, t_0}$ and $\delta \Phi_{k-1}$:

$$\mathbf{e}_{y_{k-1}}^j = \mathbf{y}_{k-1}^j - \mathbf{h}(\bar{\mathbf{p}}_{c_{k-1}}^{j, c_{k-1}}) - [\mathbf{A}_{k-1}^j \quad \mathbf{B}_{k-1}^j] \begin{bmatrix} \delta \mathbf{x} \\ \delta \mathbf{p} \end{bmatrix}, \quad (8)$$

where

$$\mathbf{A}_{k-1}^j = \mathbf{E}_{k-1} \left[-\bar{\mathbf{C}}_{c_{k-1}, t_0} \left(\bar{\mathbf{C}}_{c_{k-1}, t_0} \left(\bar{\mathbf{p}}_{t_0}^{j, t_0} - \bar{\mathbf{p}}_{t_0}^{c_{k-1}, t_0} \right) \right)^\times \quad \mathbf{0} \quad \mathbf{0} \right],$$

$$\mathbf{B}_{k-1}^j = \mathbf{E}_{k-1} \bar{\mathbf{C}}_{c_{k-1}, t_0}, \quad \mathbf{E}_{k-1} = \frac{\partial \mathbf{h}}{\partial \mathbf{p}} \bigg|_{\mathbf{p}_{c_{k-1}}^{j, c_{k-1}}}.$$

3.3.2. Sun Sensor Model

We will now outline the derivation of the sun sensor observation model, which closely resembles the one derived by Barfoot, Forbes, and Furgale (2010). After image acquisition and some postprocessing, the sun sensor determines a unit vector pointing from the sensor to the sun. This unit vector can be completely described relative to the sun sensor frame by the measurement \mathbf{s}_k , consisting of a rotation about the x -axis by angle ϕ_k and a rotation about the y -axis by θ_k . The definition of these angles is shown in Figure 3. To perform our analysis, we also define an ephemeris frame, \mathcal{F}_{e_k} , with z -axis aligned with the sun direction, $\underline{\mathbf{s}}_k$, and y -axis lying in the yz plane of the topocentric frame, \mathcal{F}_{t_0} . Additionally, we define a measurement frame, \mathcal{F}_{m_k} , with z -axis aligned with the sun direction, $\underline{\mathbf{s}}_k$, and y -axis lying in the yz plane of the sun sensor frame, \mathcal{F}_{s_k} .

Thus, we can write the set of Euler angles from our current measurement, $\tilde{\eta}_k$, as follows:

$$\mathbf{s}_k := \tilde{\eta}_k = \begin{bmatrix} \theta_k \\ \phi_k \end{bmatrix}. \quad (9)$$

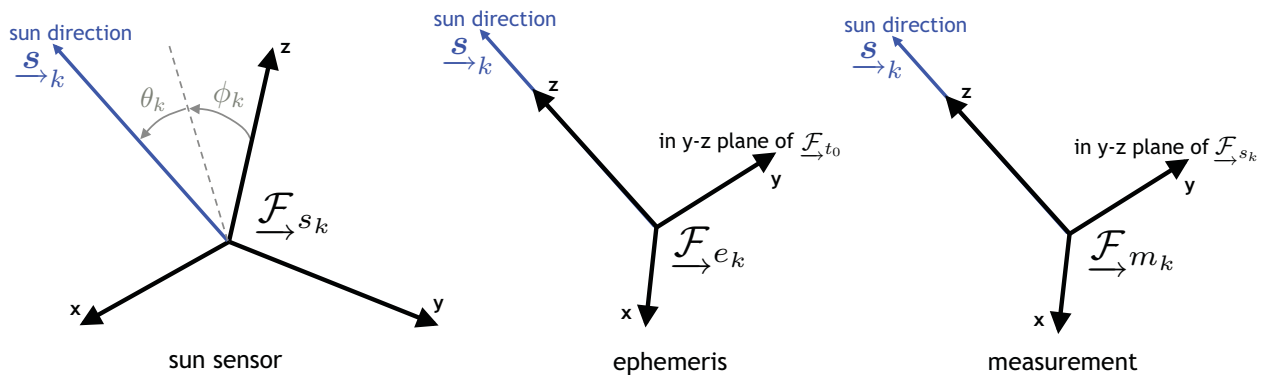


Figure 3. Definitions of the sun sensor measurement angles ϕ_k and θ_k , as well as the ephemeris and measurement frames.

Based on these angle definitions, we can define the following Euler sequence for \mathbf{C}_{s_k, m_k} , our measurement:

$$\mathbf{C}_{s_k, m_k} = \mathbf{R}_x(\phi_k) \mathbf{R}_y(\theta_k) \mathbf{R}_z(0). \quad (10)$$

We can also define an Euler sequence for \mathbf{C}_{e_k, m_k} , which is a rotation about the z -axis (of either frame) through an unknown angle, ψ_k :

$$\mathbf{C}_{e_k, m_k} = \mathbf{R}_x(0) \mathbf{R}_y(0) \mathbf{R}_z(\psi_k) \quad (11)$$

With these definitions at hand, we can now go about deriving an error term for the sun sensor measurements. Noting that \mathbf{C}_{s_k, m_k} contains the measurement information, we wish to build a predicted version of this, $\hat{\mathbf{C}}_{s_k, m_k}$. This predicted measurement will be based on our current attitude estimate relative to the topocentric frame, $\hat{\mathbf{C}}_{c_k, t_0}$, and the other interframe rotations:

$$\hat{\mathbf{C}}_{s_k, m_k} := \mathbf{C}_{c, s}^T \hat{\mathbf{C}}_{c_k, t_0} \mathbf{C}_{t_0, e_k} \mathbf{C}_{e_k, m_k}$$

$$= \mathbf{R}_x(\hat{\phi}_k) \mathbf{R}_y(\hat{\theta}_k) \mathbf{R}_z(\hat{\psi}_k).$$

Note that the rotation, \mathbf{C}_{t_0, e_k} , can be obtained from the ephemeris, the date and time of day, and an approximate knowledge of our current global position, and thus can be considered a known quantity. Also, the rotation, $\mathbf{C}_{c, s}$, is the rotation between the sun sensor and camera frames, and is assumed to be known from calibration. The angle $\hat{\psi}_k$ is nonzero because we are using $\hat{\mathbf{C}}_{c_k, t_0}$, not the true value, \mathbf{C}_{c_k, t_0} . Next, we can write the current time step attitude estimate, $\hat{\mathbf{C}}_{c_k, t_0}$, as a multiplicative perturbation about some initial estimate, $\bar{\mathbf{C}}_{c_k, t_0}$, as follows:

$$\hat{\mathbf{C}}_{s_k, m_k} \approx \mathbf{C}_{c, s}^T (\mathbf{1} - \delta \phi_k^\times) \bar{\mathbf{C}}_{c_k, t_0} \mathbf{C}_{t_0, e_k} \mathbf{C}_{e_k, m_k}$$

$$= \mathbf{C}_{c, s}^T \bar{\mathbf{C}}_{c_k, t_0} \mathbf{C}_{t_0, e_k} \mathbf{C}_{e_k, m_k} - \mathbf{C}_{c, s}^T \delta \phi_k^\times \bar{\mathbf{C}}_{c_k, t_0} \mathbf{C}_{t_0, e_k} \mathbf{C}_{e_k, m_k}.$$

Next, we insert $\mathbf{C}_{c, s} \mathbf{C}_{c, s}^T$, which is equal to identity, into the expression

$$\hat{\mathbf{C}}_{s_k, m_k} = \mathbf{C}_{c, s}^T \bar{\mathbf{C}}_{c_k, t_0} \mathbf{C}_{t_0, e_k} \mathbf{C}_{e_k, m_k}$$

$$- \mathbf{C}_{c, s}^T \delta \phi_k^\times \mathbf{C}_{c, s} \mathbf{C}_{c, s}^T \bar{\mathbf{C}}_{c_k, t_0} \mathbf{C}_{t_0, e_k} \mathbf{C}_{e_k, m_k}.$$

Using the identity $(\mathbf{C}\mathbf{r})^\times \equiv \mathbf{C}\mathbf{r}^\times \mathbf{C}^T$, we can manipulate the expression to the following forms

$$\hat{\mathbf{C}}_{s_k, m_k} = \left[\mathbf{1} - \left(\mathbf{C}_{c,s}^T \delta \boldsymbol{\phi}_k \right)^\times \right] \mathbf{C}_{c,s}^T \bar{\mathbf{C}}_{c_k, t_0} \mathbf{C}_{t_0, e_k} \mathbf{C}_{e_k, m_k}. \quad (12)$$

The compound rotation, $\mathbf{C}_{c,s}^T \bar{\mathbf{C}}_{c_k, t_0} \mathbf{C}_{t_0, e_k}$, may be expressed as the following Euler sequence:

$$\mathbf{C}_{c,s}^T \bar{\mathbf{C}}_{c_k, t_0} \mathbf{C}_{t_0, e_k} = \mathbf{R}_x(\bar{\phi}_k) \mathbf{R}_y(\bar{\theta}_k) \mathbf{R}_z(\bar{\nu}_k).$$

Thus, we can write (12) as follows:

$$\begin{aligned} \hat{\mathbf{C}}_{s_k, m_k} &= \left[\mathbf{1} - \left(\mathbf{C}_{c,s}^T \delta \boldsymbol{\phi}_k \right)^\times \right] \mathbf{R}_x(\bar{\phi}_k) \mathbf{R}_y(\bar{\theta}_k) \mathbf{R}_z(\bar{\nu}_k) \mathbf{R}_z(\psi_k) \\ &= \left[\mathbf{1} - \left(\mathbf{C}_{c,s}^T \delta \boldsymbol{\phi}_k \right)^\times \right] \mathbf{R}_x(\bar{\phi}_k) \mathbf{R}_y(\bar{\theta}_k) \mathbf{R}_z(\bar{\nu}_k + \psi_k) \\ &= \left[\mathbf{1} - \left(\mathbf{C}_{c,s}^T \delta \boldsymbol{\phi}_k \right)^\times \right] \bar{\mathbf{C}}_{s_k, m_k}, \end{aligned} \quad (13)$$

where $\bar{\mathbf{C}}_{s_k, m_k} = \mathbf{R}_x(\bar{\phi}_k) \mathbf{R}_y(\bar{\theta}_k) \mathbf{R}_z(\bar{\nu}_k + \psi_k)$. The angle ψ_k is unknown, but as we will see, we will not need it. The resulting expression for our predicted measurement is of the same linearized form as (2), with the $\delta \boldsymbol{\phi}_k$ from (2) taking the form $\mathbf{C}_{c,s}^T \delta \boldsymbol{\phi}_k$ in (13). Thus, the perturbation of the predicted measurement rotation matrix, as shown in (13), corresponds to a perturbation of the predicted measurement Euler angles, $\hat{\boldsymbol{\eta}}_k \approx \bar{\boldsymbol{\eta}}_k + \delta \boldsymbol{\eta}_k$. We can derive an expression for the perturbation $\delta \boldsymbol{\eta}_k$ using (1) and (2):

$$\begin{aligned} \mathbf{C}_{c,s}^T \delta \boldsymbol{\phi}_k &= \mathbf{S}(\bar{\boldsymbol{\eta}}_k) \delta \boldsymbol{\eta}_k \\ \Rightarrow \delta \boldsymbol{\eta}_k &= \mathbf{S}^{-1}(\bar{\boldsymbol{\eta}}_k) \mathbf{C}_{c,s}^T \delta \boldsymbol{\phi}_k. \end{aligned} \quad (14)$$

Thus, the expression for the perturbed predicted measurement in Euler angles is as follows:

$$\hat{\boldsymbol{\eta}}_k = \bar{\boldsymbol{\eta}}_k + \mathbf{S}^{-1}(\bar{\boldsymbol{\eta}}_k) \mathbf{C}_{c,s}^T \delta \boldsymbol{\phi}_k, \quad (15)$$

where

$$\hat{\boldsymbol{\eta}}_k := \begin{bmatrix} \hat{\nu}_k \\ \hat{\theta}_k \\ \hat{\phi}_k \end{bmatrix}, \quad \bar{\boldsymbol{\eta}}_k := \begin{bmatrix} \bar{\nu}_k + \psi_k \\ \bar{\theta}_k \\ \bar{\phi}_k \end{bmatrix},$$

$$\mathbf{S}(\bar{\boldsymbol{\eta}}_k) := [\mathbf{R}_x(\bar{\phi}_k) \mathbf{R}_y(\bar{\theta}_k) \mathbf{1}_3 \quad \mathbf{R}_x(\bar{\phi}_k) \mathbf{1}_2 \quad \mathbf{1}_1],$$

and where $\mathbf{1}_i$ represents the i th column of $\mathbf{1}$. Note that the unknown angles $\bar{\nu}_k$ and ψ_k are not used in the calculation of $\mathbf{S}(\bar{\boldsymbol{\eta}}_k)$, because of our selection of Euler sequence. Additionally, our selection of Euler sequence has its singularity at $\theta_k = \pi/2$, which is out of the field of view of our sensor. We note, however, that our Euler angle terms consist of three unique angles, whereas our measurements consist of only two angles. To put our error expression in the same terms as our measurements, we utilize a projection matrix, \mathbf{P} , of the following form:

$$\mathbf{P} := \begin{bmatrix} 0 & 1 & 0 \\ 0 & 0 & 1 \end{bmatrix}.$$

Multiplying (15) by this projection matrix gives us the predicted sun sensor measurement in two Euler angles. Note that the appli-

cation of the projection matrix makes the values of the unknown angles, $\bar{\nu}_k$ and ψ_k , irrelevant. We can now write our final linearized expression for the sun sensor measurement error:

$$\begin{aligned} \mathbf{e}_{s_k} &= (\mathbf{s}_k - \hat{\boldsymbol{\eta}}_k) \\ &= \mathbf{s}_k - \mathbf{P} \left(\bar{\boldsymbol{\eta}}_k - \mathbf{S}^{-1}(\bar{\boldsymbol{\eta}}_k) \mathbf{C}_{c,s}^T \delta \boldsymbol{\phi}_k \right). \end{aligned} \quad (16)$$

We can reexpress the error term in matrix form as follows:

$$\mathbf{e}_{s_k} = \mathbf{s}_k - \mathbf{P} \bar{\boldsymbol{\eta}}_k + \mathbf{U} \delta \mathbf{x}, \quad (17)$$

where

$$\mathbf{U} = [\mathbf{0} \quad \mathbf{0} \quad \mathbf{0} \quad \mathbf{P} \mathbf{S}^{-1}(\bar{\boldsymbol{\eta}}_k) \mathbf{C}_{c,s}^T].$$

3.3.3. Inclinometer Model

The process of deriving the inclinometer model is essentially the same as for the sun sensor, so we present a very brief summary of the main concepts here. The inclinometer is measuring the pitch angle, β_k , and roll angle, γ_k , of the inclinometer with respect to the topocentric frame. The definition of these angles is shown in Figure 4, where we have shown the angles measured relative to the negative gravity vector, which is equivalent to the negative z -axis of the topocentric frame. We also define a measurement frame, \mathcal{F}_{n_k} , with z -axis aligned with the negative gravity direction, \mathbf{g} , and y -axis lying in the yz -plane of the inclinometer frame, \mathcal{F}_{g_k} . Thus, we can write the set of Euler angles from our current measurement, $\tilde{\boldsymbol{\eta}}_k$, as follows:

$$\mathbf{g}_k := \tilde{\boldsymbol{\eta}}_k = \begin{bmatrix} \beta_k \\ \gamma_k \end{bmatrix}. \quad (18)$$

Based on these angle definitions, we can define the following Euler sequence for \mathbf{C}_{g_k, n_k} , our measurement:

$$\mathbf{C}_{g_k, n_k} = \mathbf{R}_x(\gamma_k) \mathbf{R}_y(\beta_k) \mathbf{R}_z(0).$$

We can also define an Euler sequence for \mathbf{C}_{t_0, n_k} , which is a rotation about the z -axis (of either frame) through an unknown angle, ψ_k :

$$\mathbf{C}_{t_0, n_k} = \mathbf{R}_x(0) \mathbf{R}_y(0) \mathbf{R}_z(\psi_k).$$

Noting that \mathbf{C}_{g_k, n_k} contains the measurement information, we can build a predicted version of this, $\hat{\mathbf{C}}_{g_k, n_k}$. This predicted measurement will be based on our current attitude estimate relative to the topocentric frame, $\bar{\mathbf{C}}_{c_k, t_0}$, and the other interframe rotations:

$$\begin{aligned} \hat{\mathbf{C}}_{g_k, n_k} &:= \mathbf{C}_{c,g}^T \hat{\mathbf{C}}_{c_k, t_0} \mathbf{C}_{t_0, n_k} \\ &= \mathbf{R}_x(\hat{\gamma}_k) \mathbf{R}_y(\hat{\beta}_k) \mathbf{R}_z(\hat{\nu}_k). \end{aligned}$$

Following the same procedure as outlined in the sun sensor model subsection, the linearized inclinometer error term can be determined from the above equations as follows:

$$\mathbf{e}_{g_k} = \mathbf{g}_k - \mathbf{P} \left(\bar{\boldsymbol{\eta}}_k - \mathbf{S}^{-1}(\bar{\boldsymbol{\eta}}_k) \mathbf{C}_{c,g}^T \delta \boldsymbol{\phi}_k \right). \quad (19)$$

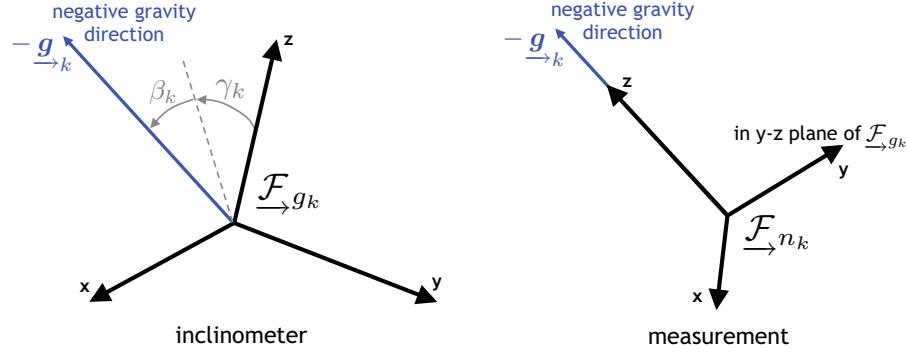


Figure 4. Definitions of the inclinometer measurements angle β_k and γ_k , as well as the measurement frame.

We can reexpress the error term in matrix form as follows:

$$\mathbf{e}_{g_k} = \mathbf{g}_k - \mathbf{P} \bar{\eta}_k + \mathbf{G} \delta \mathbf{x}, \quad (20)$$

where

$$\mathbf{G} = \begin{bmatrix} \mathbf{0} & \mathbf{0} & \mathbf{0} & \mathbf{P} \mathbf{S}^{-1}(\bar{\eta}_k) \mathbf{C}_{c,g}^T \end{bmatrix}. \quad (21)$$

We note that (17) and (20) are of the same form, because both the sun and gravity directions are vector measurements described by a pair of rotations about the x - and y -axes.

3.3.4. Prior Term

As previously mentioned, because our sun sensor and inclinometer measurement error terms require a current estimate of the vehicle orientation relative to the topocentric frame, we solve for the states relative to \mathcal{F}_{t_0} . To constrain this solution in space, we include a prior on the state variables based on the estimate up to the current time; this bundle adjustment implementation is functionally similar to the iterated EKF. We start by taking our estimate of the state resulting from the bundle adjustment solution at the previous time step and reframing it as a prior incorporating the information from all our measurements up to the time $k-1$ (at the end of Section 3.4, we will show how this prior is determined from the estimated quantities at a given time step). We denote this term as $\hat{\mathbf{x}} = \{\hat{\mathbf{C}}_{c_{k-1}, t_0}, \hat{\mathbf{p}}_{t_0}^{c_{k-1}, t_0}\}$, with 6×6 covariance matrix \mathbf{T}_{k-1} . With this prior defined, we go about deriving the error terms for the translation and rotation elements of the vehicle state.

For the translational terms, we start by defining the error between the prior and the true state as $\delta \hat{\mathbf{p}}_{t_0}^{c_{k-1}, t_0}$, which we assume to be a small perturbation. The covariance of this error, $E[\delta \hat{\mathbf{p}}_{t_0}^{c_{k-1}, t_0} \delta \hat{\mathbf{p}}_{t_0}^{c_{k-1}, t_0 T}]$, is described by the 3×3 upper left-hand corner of \mathbf{T}_{k-1} . With these definitions at hand, we can write the following expression for the true state:

$$\mathbf{p}_{t_0}^{c_{k-1}, t_0} \approx \hat{\mathbf{p}}_{t_0}^{c_{k-1}, t_0} + \delta \hat{\mathbf{p}}_{t_0}^{c_{k-1}, t_0}. \quad (22)$$

Following a similar logic, we can also express the true translational state using our current state estimate plus some error perturbation:

$$\mathbf{p}_{t_0}^{c_{k-1}, t_0} \approx \bar{\mathbf{p}}_{t_0}^{c_{k-1}, t_0} + \delta \mathbf{p}_{t_0}^{c_{k-1}, t_0}. \quad (23)$$

By equating (22) and (23) and rearranging some terms, we can arrive at an error expression for the translational prior:

$$\mathbf{e}_{k-1, \text{trans}} := \delta \hat{\mathbf{p}}_{t_0}^{c_{k-1}, t_0} = \bar{\mathbf{p}}_{t_0}^{c_{k-1}, t_0} - \hat{\mathbf{p}}_{t_0}^{c_{k-1}, t_0} + \delta \mathbf{p}_{t_0}^{c_{k-1}, t_0}. \quad (24)$$

The rotational prior error can be derived in a similar, albeit slightly more complicated, fashion. We start by defining the error between the prior and the true state as the rotation vector $\delta \psi_{k-1}$, which we assume to be a small perturbation:

$$\delta \psi_{k-1}^\times := \mathbf{1} - \mathbf{C}_{c_{k-1}, t_0} \hat{\mathbf{C}}_{c_{k-1}, t_0}^T. \quad (25)$$

The covariance of this error, $E[\delta \psi_{k-1} \delta \psi_{k-1}^T]$, is described by the 3×3 lower right-hand corner of \mathbf{T}_{k-1} . We can also express the true rotational state as a perturbation of our current state estimate:

$$\mathbf{C}_{c_{k-1}, t_0} \approx (\mathbf{1} - \delta \Phi_{k-1}^\times) \bar{\mathbf{C}}_{c_{k-1}, t_0}. \quad (26)$$

We can combine these two expressions by substituting (26) into (25):

$$\delta \psi_{k-1}^\times = \mathbf{1} - (\mathbf{1} - \delta \Phi_{k-1}^\times) \bar{\mathbf{C}}_{c_{k-1}, t_0} \hat{\mathbf{C}}_{c_{k-1}, t_0}^T. \quad (27)$$

Noticing that the $\bar{\mathbf{C}}_{c_{k-1}, t_0} \hat{\mathbf{C}}_{c_{k-1}, t_0}^T$ term will be small, we can make the following approximation:

$$\bar{\mathbf{C}}_{c_{k-1}, t_0} \hat{\mathbf{C}}_{c_{k-1}, t_0}^T \approx \mathbf{1} - \delta \xi_{k-1}^\times, \quad (28)$$

where $\delta \xi_{k-1}$ can be determined by computing the value of $\mathbf{1} - \bar{\mathbf{C}}_{c_{k-1}, t_0} \hat{\mathbf{C}}_{c_{k-1}, t_0}^T = \delta \xi_{k-1}^\times$ and picking out the elements of $\delta \xi_{k-1}$ from the resulting matrix. Substituting (28) into (27) and eliminating products of small perturbations yields

$$\delta \psi_{k-1}^\times = \delta \Phi_{k-1}^\times + \delta \xi_{k-1}^\times.$$

Applying the identity $\mathbf{a}^\times + \mathbf{b}^\times \equiv (\mathbf{a} + \mathbf{b})^\times$, we arrive at our final error expression for the rotational state prior,

$$\mathbf{e}_{k-1, \text{rot}} := \delta \psi_{k-1} = \delta \xi_{k-1} + \delta \Phi_{k-1}. \quad (29)$$

To use these error terms in the bundle adjustment solution, we also define the following matrices:

$$\mathbf{e}_{k-1} = \begin{bmatrix} \mathbf{e}_{k-1}^{\text{trans}} \\ \mathbf{e}_{k-1}^{\text{rot}} \end{bmatrix}, \quad \mathbf{R} = \begin{bmatrix} \mathbf{1} & \mathbf{0} & \mathbf{0} & \mathbf{0} \\ \mathbf{0} & \mathbf{1} & \mathbf{0} & \mathbf{0} \end{bmatrix}.$$

It is worth pointing out that our formulation applies a prior only to the vehicle state and not to the landmarks. Because there is no prior introduced on the landmarks, we have not accounted for the fact that key points may be matched at multiple frames; in other words, we run the risk of overtrusting measurements. However, this is an inherent risk in any frame-to-frame VO system, where the additional complexity of carrying forward landmark estimates through time is undesirable. It is important to note that, although frame-to-frame bundle adjustment provides a good estimation framework for our application, the sun sensor and inclinometer error terms derived in this paper could be incorporated into any number of solution methods. This landmark uncertainty issue could be resolved by using the sun sensor and inclinometer measurements within a full simultaneous localization and mapping (SLAM) solution. However, this approach falls beyond the scope of this paper, as our goal was to improve accuracy without increasing computational cost significantly.

3.4. Bundle Adjustment Solution

Using our linearized error terms from above, we can construct our objective function, which we will minimize to obtain the maximum likelihood estimate for our new vehicle state:

$$\mathbf{J}(\mathbf{x}, \mathbf{p}) := \frac{1}{2} (\mathbf{e}_{k-1}^T \mathbf{T}_{k-1}^{-1} \mathbf{e}_{k-1} + \mathbf{e}_g^T \mathbf{T}_g^{-1} \mathbf{e}_g + \mathbf{e}_s^T \mathbf{T}_s^{-1} \mathbf{e}_s + \mathbf{e}_y^T \mathbf{T}_y^{-1} \mathbf{e}_y), \quad (30)$$

where \mathbf{T}_{k-1}^{-1} , \mathbf{T}_g^{-1} , \mathbf{T}_s^{-1} , and \mathbf{T}_y^{-1} represent the inverse covariance matrices for the previous state, inclinometer, sun sensor, and stereo feature measurements, respectively. We can minimize this objective function using Gauss–Newton optimization. An update step in the optimization process can be determined by augmenting the classic bundle adjustment update step as follows:

$$\mathbf{H}^T \mathbf{T}^{-1} \mathbf{H} \begin{bmatrix} \delta \mathbf{x} \\ \delta \mathbf{p} \end{bmatrix} = -\mathbf{H}^T \mathbf{T}^{-1} \mathbf{e}(\bar{\mathbf{x}}, \bar{\mathbf{p}}), \quad (31)$$

where

$$\mathbf{H} := \begin{bmatrix} \mathbf{R} & \mathbf{0} \\ \mathbf{G} & \mathbf{0} \\ \mathbf{U} & \mathbf{0} \\ \mathbf{A} & \mathbf{B} \end{bmatrix}, \quad \mathbf{T}^{-1} := \text{diag} \left\{ \mathbf{T}_{k-1}^{-1}, \mathbf{T}_g^{-1}, \mathbf{T}_s^{-1}, \mathbf{T}_y^{-1} \right\},$$

and where \mathbf{A} and \mathbf{B} incorporate each of the Jacobians \mathbf{A}_k^j and \mathbf{B}_k^j for the key points observed at time k as well as the Jacobians \mathbf{A}_{k-1}^j and \mathbf{B}_{k-1}^j for the same key points observed at time $k-1$.

Constructing the left-hand side, we have

$$\mathbf{H}^T \mathbf{T}^{-1} \mathbf{H} = \begin{bmatrix} \mathbf{R}^T \mathbf{T}_{k-1}^{-1} \mathbf{R} + \mathbf{G}^T \mathbf{T}_g^{-1} \mathbf{G} + \mathbf{U}^T \mathbf{T}_s^{-1} \mathbf{U} + \mathbf{A}^T \mathbf{T}_y^{-1} \mathbf{A} & \mathbf{A}^T \mathbf{T}_y^{-1} \mathbf{B} \\ \mathbf{B}^T \mathbf{T}_y^{-1} \mathbf{A} & \mathbf{B}^T \mathbf{T}_y^{-1} \mathbf{B} \end{bmatrix}, \quad (32)$$

where the matrix is partitioned into the pose and landmark components. We can explicitly illustrate the contributions of the stereo camera, prior, sun sensor, and inclinometer terms by rewriting (32) as a sum:

$$\mathbf{H}^T \mathbf{T}^{-1} \mathbf{H} = \underbrace{\begin{bmatrix} \mathbf{A}^T \mathbf{T}_y^{-1} \mathbf{A} & \mathbf{A}^T \mathbf{T}_y^{-1} \mathbf{B} \\ \mathbf{B}^T \mathbf{T}_y^{-1} \mathbf{A} & \mathbf{B}^T \mathbf{T}_y^{-1} \mathbf{B} \end{bmatrix}}_{\text{stereo camera terms}} + \underbrace{\begin{bmatrix} \mathbf{R}^T \mathbf{T}_{k-1}^{-1} \mathbf{R} + \mathbf{G}^T \mathbf{T}_g^{-1} \mathbf{G} + \mathbf{U}^T \mathbf{T}_s^{-1} \mathbf{U} & \mathbf{0} \\ \mathbf{0} & \mathbf{0} \end{bmatrix}}_{\text{prior, sun sensor, and inclinometer terms}}. \quad (33)$$

From (33), we can see that the inclusion of the additional measurements does not disturb the sparse structure of the bundle adjustment problem. The prior, sun sensor, and inclinometer terms are block diagonal (as shown in Figure 5(b)), and are added to the upper left corner of the stereo camera terms, which are also block diagonal (see Figure 5(a)). Thus, as shown in Figure 5(c), the sparse structure is preserved, allowing computationally efficient sparse methods to be used for solving (Brown, 1958).

We determine the state at time k , $\{\mathbf{C}_{c_k, t_0}, \mathbf{p}_{t_0}^{c_k, t_0}\}$, through an iterative sequence of update steps, per Gauss–Newton (note that although we also solve for the state at time $k-1$, the new estimate is discarded, as it was necessary only to allow the addition of the prior term):

1. Using the current estimated values for $\{\mathbf{C}_{c_k, t_0}, \mathbf{p}_{t_0}^{c_k, t_0}\}$, $\{\mathbf{C}_{c_{k-1}, t_0}, \mathbf{p}_{t_0}^{c_{k-1}, t_0}\}$, and $\mathbf{p}_{t_0}^{j, t_0}$, compute an update step $[\delta \mathbf{x}^T \delta \mathbf{p}^T]^T$ by solving Eq. (31) using sparse bundle adjustment methods.
2. Check for convergence. If converged, stop; otherwise continue to Step 3.
3. The state and feature position updates are then applied to $\{\mathbf{C}_{c_k, t_0}, \mathbf{p}_{t_0}^{c_k, t_0}\}$, $\{\mathbf{C}_{c_{k-1}, t_0}, \mathbf{p}_{t_0}^{c_{k-1}, t_0}\}$, and $\mathbf{p}_{t_0}^{j, t_0}$, respectively, according to

$$\begin{aligned} \mathbf{C}_{c_k, t_0} &\leftarrow \Phi_k \mathbf{C}_{c_k, t_0}, \\ \mathbf{p}_{t_0}^{c_k, t_0} &\leftarrow \mathbf{p}_{t_0}^{c_k, t_0} + \delta \mathbf{p}_{t_0}^{c_k, t_0}, \\ \mathbf{p}_{t_0}^{j, t_0} &\leftarrow \mathbf{p}_{t_0}^{j, t_0} + \delta \mathbf{p}_{t_0}^{j, t_0}, \end{aligned}$$

where

$$\Phi_k = \cos(\delta \phi_k) \mathbf{1} + (1 - \cos(\delta \phi_k)) \left(\frac{\delta \Phi_k}{\delta \phi_k} \right) \left(\frac{\delta \Phi_k}{\delta \phi_k} \right)^T$$

$$- \sin(\delta \phi_k) \left(\frac{\delta \Phi_k}{\delta \phi_k} \right)^\times$$

and $\delta \phi_k := |\delta \Phi_k|$.

4. Return to Step 1.

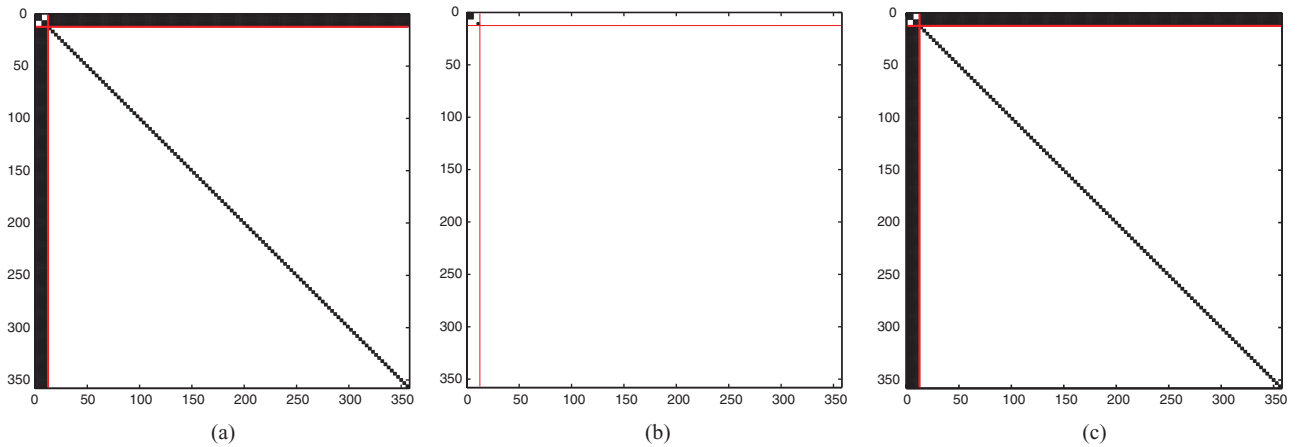


Figure 5. The actual sparsity pattern of the $\mathbf{H}^T \mathbf{T}^{-1} \mathbf{H}$ matrix from one time step of our data set, showing contributions from the stereo camera, prior, sun sensor, and inclinometer terms. Black indicates an occupied element, whereas white represents a zero. The red lines indicate the block partitioning shown in (32) and (33). (a) Contribution of stereo camera terms, as in (33). (b) Contribution of prior, sun sensor, and inclinometer terms, as in (33). (c) Summed matrix with all terms, as in (32).

Upon convergence, we obtain our maximum likelihood estimate for the current state at time k , $\{\hat{\mathbf{C}}_{c_k, t_0}, \hat{\mathbf{p}}_{t_0}^{c_k, t_0}\}$. Additionally, the 6×6 covariance matrix corresponding to this state, \mathbf{T}_k , is computed as part of the sparse bundle adjustment solution. With this information in hand, we can form the prior term that will be used at the next time step, $k + 1$. The current state estimate, $\{\hat{\mathbf{C}}_{c_k, t_0}, \hat{\mathbf{p}}_{t_0}^{c_k, t_0}\}$, is redefined at the next time step as the prior term, $\hat{\mathbf{x}} = \{\hat{\mathbf{C}}_{c_{k-1}, t_0}, \hat{\mathbf{p}}_{t_0}^{c_{k-1}, t_0}\}$. Similarly, the covariance matrix for the current state, \mathbf{T}_k , is used as the covariance matrix of the prior, \mathbf{T}_{k-1} .

This formulation allows us to incorporate sun sensor and inclinometer measurements directly into the visual odometry solution as we acquire them. Note that we do not require both or any sun vector and gravity measurements at a given time step; any measurements that are available can be individually included in the bundle adjustment solution. Thus, whenever possible, we are continuously correcting the camera orientation using absolute information, preventing the aggregation of errors over time. If there are no absolute orientation measurements at that time step, the bundle adjustment will proceed as usual, solving for the camera transformation using only the stereo key points.

4. DESCRIPTION OF FIELD EXPERIMENTS

To test our VO algorithm with sun sensor and inclinometer measurements, extensive data were collected during a 10-km rover traverse in a Mars analogue environment on Devon Island. The recorded data have been processed and packaged into a complete data set (Furgale, Carle, Enright, & Barfoot, 2012), including stereo images, sun vectors, inclinometer gravity vectors, and GPS ground truth for position. The details of this data set are presented in this section, including particulars of the traverse and the hardware configuration.

4.1. Scenario Description

Our data collection took place near the Haughton-Mars Project Research Station (HMPRS) ($75^\circ 22'$ N latitude and $89^\circ 41'$ W longitude) on Devon Island in the Canadian high Arctic. The site is considered to be a strong analog for planetary environments (Lee et al., 1998) because of its geological makeup and vegetation-free desert landscape, as seen in Figures 1 and 6. A pushcart rover platform traversed a 10-km loop through rugged canyons, sandy flats, and high-grade slopes over a period of 10 h. To illustrate the path of the pushcart rover, Figure 7 shows the entire traverse loop plotted in Google Earth. The test was performed in July 2008; the Arctic sun remained above the horizon line for 24 h a day.

The 10-km loop has been partitioned into 23 sections of varying length, labeled with indices from 0 to 22. At the beginning of each of the individual sections, the rover platform remained stationary for a few minutes to collect large amounts of sun sensor and inclinometer data. These measurements have been used to provide periodic updates of the platform orientation for the full 10-km estimated traverse (Enright, Furgale, & Barfoot, 2009). It would also be possible to use these computed orientations to initialize the rover attitude of each VO path estimate, but any small angular error in the initial heading between our estimated path and our ground truth path will lead to errors of hundreds of meters over the course. To make the error reporting as accurate as possible, we have aligned the first 50 m of each estimated section traverse with GPS ground truth and then calculated the error on the remaining length of the traverse. This ensures that we are reporting the positional error accumulated by VO along the traverse path, and not reporting errors due to inaccurate initial heading. Positional ground truth was provided by a pair of Magellan ProMark3 GPS units, which were used to produce postprocessed differential GPS for the whole traverse. These measures of rover platform position and orientation allow us to assess the accuracy of our motion estimates confidently from VO.

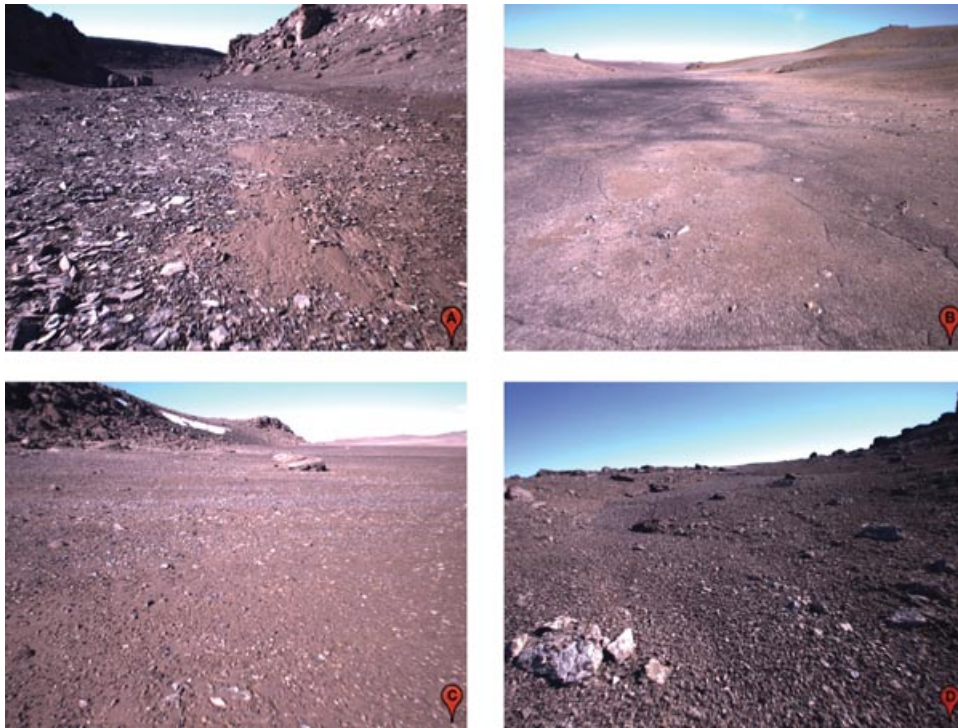


Figure 6. Typical images acquired by the left camera of the stereo pair during the 10-km traverse of Devon Island. Note that for our experiments, we used 512×384 gray scale versions of the images. The letter labels are used to identify the image locations in Figure 7.

4.2. Hardware Configuration

The data set was collected using a pushcart platform outfitted with a suite of rover engineering sensors, as seen in Figure 8(a). Because our VO technique does not use any wheel odometry or rover telemetry data, the unactuated nature of the platform has no effect on our motion estimation. The stereo camera was a Point Grey Research Bumblebee XB3 with a baseline of 24 cm and a 70-deg field of view, mounted approximately 1 m above the surface pointing downward by approximately 20 deg. Over the course of the 10-km traverse, the stereo camera acquired 49,410 images, which have been processed to 512×384 rectified greyscale images for these experiments. Color versions of some typical images from the data set are presented in Figure 6, further illustrating the Mars-like nature of the terrain. The inclinometer was a Honeywell HMR-3000, which weighs only 90 g and uses a fluid tilt sensor to estimate the direction of gravity. Because the sensor directly outputs gravity vectors, the rover computer does not have to perform any expensive computation to produce these measurements.

The sun sensor used in these experiments is a Sinclair Interplanetary SS-411 digital sun sensor, as shown in Figure 8(b). It is a low-power, low-mass device designed for use on microsatellites, weighing only 34 g. A linear pixel array is used to capture an image, which is then processed by an integrated microcontroller to output floating point sun vector measurements in the sensor frame (Enright & Sinclair, 2007). Because the processing is done onboard by the sensor, producing sun vector measurements is of

minimal computational cost to the rover computer. Additionally, the sensor monitors the quality of the detected images, rejecting poor-quality images that can be caused by clouds or other factors. This produces intermittent gaps in the sun sensor data, which can subsequently affect our motion estimate. However, our VO framework is flexible enough to incorporate sun measurements when available and rely entirely on stereo vision when not.

5. EXPERIMENTAL RESULTS

We will now present the experimental results produced by running our algorithm, as previously outlined in Section 3, offline on the 10-km loop data set from Devon Island. Motion estimates were calculated for each of the 23 individual sections of the traverse, allowing us to illustrate statistical trends on a large set of data. First, we evaluate the performance of three stereo feature detectors on the images from the Mars analog environment. Next, we examine the contributions of the sun sensor and inclinometer and demonstrate the improved localization accuracy using both sensors on individual and concatenated sections. Finally, we present results illustrating how our algorithm can be used to decrease the number of images required by VO, thereby reducing its computational burden.

5.1. Evaluating Feature Detectors

Once an image has been acquired from the stereo camera and processed into a usable form, the first step in the VO pipeline



Figure 7. The 10-km traverse loop plotted in Google Earth. The starting points for the 23 individual sections are shown, as well as the locations of the images from Figure 6.

is to extract key points in the image. These key points are matched between the left and right images of a stereo frame and tracked through time in stereo frames acquired at consecutive timesteps, and outliers are removed using RANSAC (a standard

approach for VO). A number of different feature detectors have been employed for this task in the literature, each with its own unique properties. As discussed in Section 2, the Mars exploration rovers use the Harris corner detector, which uses the autocorrelation function to measure changes in image intensity that result from shifting the image patch (Harris & Stephens, 1988). Harris corners are simple to compute, and thus are well suited for computationally limited planetary exploration rovers. Another computationally efficient method is the FAST (features from accelerated segment test) feature detector (Rosten & Drummond, 2005, 2006). In this algorithm, a circle of pixels surrounding a candidate point is examined, and a feature is detected if a certain number of these contiguous pixels are above or below the intensity of the candidate by some threshold. The FAST detector was recently employed by Sibley, Mei, Reid, and Newman (2010) in a real-time relative SLAM system. Another option is the SURF (speeded up robust features) detector (Bay, Ess, Tuytelaars, & Gool, 2008), which uses integral images and a Hessian matrix approximation to detect bloblike structures on multiple scales. An implementation of the SURF algorithm for graphics processing units (GPUs) was recently utilized by Furgale and Barfoot (2010) for a visual-teach-and-repeat system.

In order to evaluate which of these three detectors would perform best on our data, we ran our VO algorithm (without sun sensor and inclinometer measurements) on all 23 individual sections of the data set using each of the detectors. To make the comparison as fair as possible, we adjusted the parameters of the detectors such that each produced approximately the same number of detected key points for a given image, which were then passed to identical stereo matching and tracking algorithms. Also, for this comparison test, we did not utilize the key point scale values outputted by the SURF detector in any way, to maintain a level playing field.

The results for each detector are shown in Figure 9, where the XYZ (i.e., Euclidean) error growth curves are shown for all

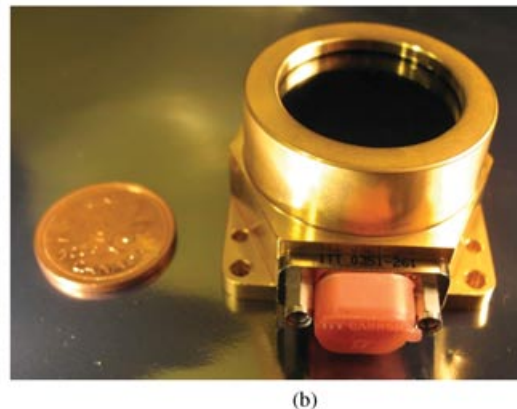
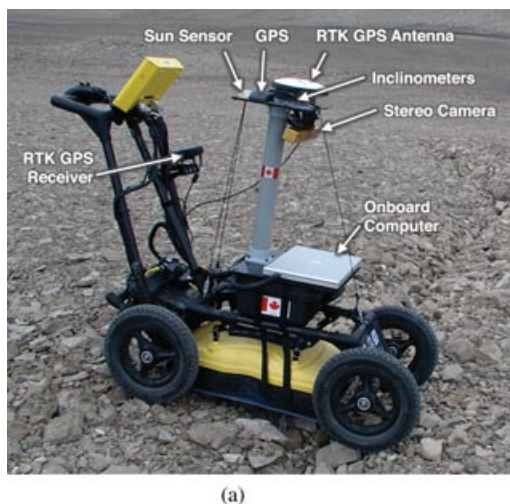


Figure 8. The key hardware utilized in our field trials on Devon Island. (a) The pushcart rover platform at Devon Island. (b) Sinclair Interplanetary SS-411 digital sun sensor.

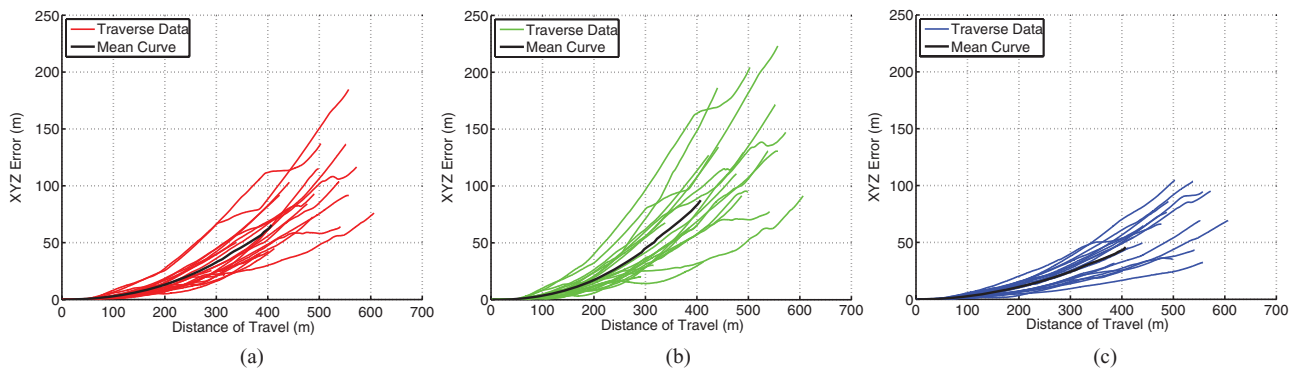


Figure 9. XYZ error as a function of distance for all individual traverses, using the three feature detectors. Mean error curves have been included to aid comparison. (a) Harris, (b) FAST, (c) SURF.

23 individual traverse sections. Additionally, to aid comparison between detectors, we have computed and plotted the mean error curves for the 23 traverse sections in Figure 10(a). In the interest of smoothness, the mean values were calculated in 5-m windows, and have only been computed up to a distance of travel where there are data available from 15 trials. As previously mentioned, for the purpose of accurate error reporting, we have aligned the first 50 m of each estimated path with ground truth and then calculated the error on the remainder of the traverse. It is also important to note that some parameters in the algorithm required tuning, such as the disparity threshold for the stereo feature measurements. These values were tuned to optimize performance on Section 0, and then those tuned parameters were retained for use with every other section. This procedure is similar to any field trial, in which parameters can be tuned based on a known set of data and then tested experimentally in the field. From Figure 9, we observe that some of the sections were quite challenging, producing large errors compared to what have typically been reported in the literature. It is important to note that we are testing our tech-

nique on long-distance traverses, over which the error of visual odometry is superlinearly increasing. Also, the challenging sections of the traverse often consisted of long stretches of flat terrain covered in small, pebblelike rocks. These flat, uniform landscapes are representative of common planetary environments, but they make rich feature detection difficult, producing the results we have observed. Also, in contrast to some of the more accurate techniques presented in the literature (Konolige et al., 2007; Mei et al., 2011), we are simply using frame-to-frame stereo matching, rather than a multiframe approach. Overall, the results indicate that the SURF detector is best suited to our challenging planetary analog terrain, as observed in Figure 10(a).

5.2. Using Feature Scale

Given these results, we have selected the SURF detector to use in all our following VO experiments incorporating a sun sensor and inclinometer. However, we first wish to examine whether we can further improve the accuracy of our motion estimates by utilizing

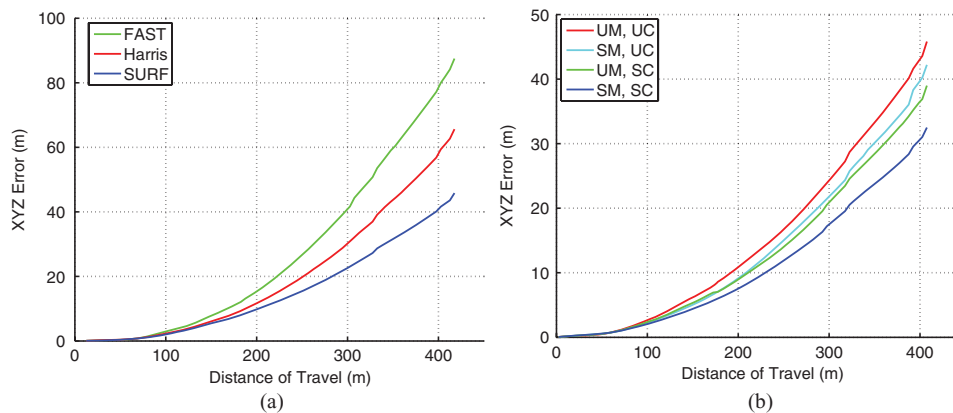


Figure 10. Mean XYZ error curves for all 23 traverse sections to aid comparison between the variations on feature tracking and scale. (a) Mean error curves for the FAST, Harris, and SURF feature detectors. (b) Mean error curves for uniform matching and uniform covariance (UM, UC), scale matching and uniform covariance (SM, UC), uniform matching and scale covariance (UM, SC), and scale matching and scale covariance (SM, SC), all using SURF features.

the key-point-scale information to our advantage. The scale gives us some sense of our uncertainty in the location of the key point; specifically, a small key-point scale indicates that the location of that feature in the image is known with little uncertainty, whereas a large key-point scale implies great uncertainty. One way to use this information is to compute the covariance for each keypoint as a function of the key-point scale, and employ each scale-specific covariance in the bundle adjustment solution. We can also use the scale information in the stereo matching step. Normally, we impose some threshold for how much a key point observed in left and right stereo images can violate the epipolar constraint, while still being considered a valid key point. Usually, this matching is performed with a uniform threshold over all key-point scales, but a better approach would be to make this threshold a function of the keypoint uncertainty, or scale. We tested the effects of key-point-scale-based matching and covariance by computing visual odometry solutions using the same 23 traverse sections, producing the mean error curves presented in Figure 10(b). We observe that employing the scale information in both of these techniques produces slightly more accurate motion estimates at minimal additional cost. Thus, these modifications will be used for the following experiments as well.

5.3. Evaluating the Effects of the Sun Sensor and Inclinometer

In this section, we present the motion estimates for each of the 23 sections produced by visual odometry incorporating sun sensor and inclinometer measurements. As determined in the above sections, these experiments were performed using the SURF feature detector with scale-based key-point matching and covariance. We compare these results against the motion estimate produced using visual odometry only. Once again, the first 50-m segment of the estimated path is aligned with ground truth, and all parameters are tuned on the first section and held constant for the remaining sections. The results are summarized in Table I, with the three-dimensional motion estimate error being expressed as a percentage of the total traversal distance.

From these results, we observe that, statistically, the addition of sun sensor and inclinometer measurements produces a much better motion estimate, often dramatically so. The most striking thing about this improvement is that it comes at a very low cost. The rover need not perform any computation to acquire the measurement vectors, and because there are many more stereo key points than sun or gravity vectors, the additional cost of bundle adjustment is almost negligible. A simple timing analysis using our MATLAB implementation showed that including the sun sensor and inclinometer measurements increased the computation time by approximately 0.3%. Given that our implementation is not currently optimized for speed, this is not meant to be taken as a formal timing test, but as an anecdotal demonstration that these additional measurements do not add a heavy computational burden to standard bundle adjustment.

The effect of the sun sensor and inclinometer is further illustrated when the XYZ error of the motion estimates is plotted as a function of distance traversed. Figure 11(a) shows that

Table I. VO XYZ error, with and without sun sensor and inclinometer, expressed as percentage of traversal distance for individual sections.

Section	Distance (m)	VO (%)	VO-SS-Inc (%)
0	413	1.6	1.3
1	477	5.4	2.1
2	606	2.3	0.8
3	541	8.1	1.4
4	402	5.0	1.2
5	552	9.4	0.7
6	538	11.3	2.0
7	499	10.2	1.4
8	444	9.0	1.3
9	487	7.6	1.8
10	572	10.2	1.0
11	386	5.3	0.7
12	557	17.5	1.1
13	490	14.9	1.5
14	442	12.6	1.7
15	557	9.0	1.1
16	503	15.7	3.5
17	423	12.2	1.4
18	338	6.5	1.0
19	316	4.0	1.0
20	296	3.7	1.9
21	170	3.0	2.0
22	124	1.3	1.4

the error of VO grows superlinearly with distance. As previously discussed, this is because small orientation errors become amplified into large position errors over long distances. In contrast, Figure 11(b) shows that sun sensor and inclinometer measurements limit the error growth significantly on a large set of unique traverses. The constant orientation corrections from the sun sensor and inclinometer keep the platform attitude close to true, preventing the amplification of errors. For ease of comparison, we have also included mean error curves computed in the same fashion as in Section 5.1. (mean values were calculated in 5-m windows, and have only been computed up to a distance of travel where there are data available from 15 trials).

In terms of the specific contributions of the sun sensor and inclinometer, the sun sensor will mainly provide information about the vehicle heading, and the inclinometer largely about the pitch and roll. However, both sensors provide some measure of the full attitude of the rover. This is because, over the course of a traverse, the ground undulates and the sun moves in the sky, so the sensors will be measuring a continuous sequence of nonparallel vectors. In our experiments, we have found that the combination of both sensors greatly outperforms the use of either the sun sensor or the inclinometer alone. This is not only because we are obtaining two distinct sets of vectors in nearly perpendicular directions, but also because we can apply more frequent corrections.

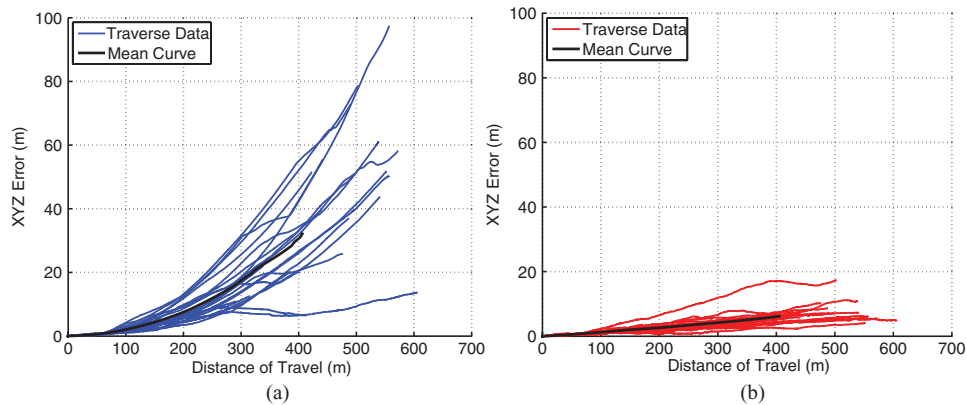


Figure 11. XYZ error as a function of distance for all individual traverses, with mean error curves included. (a) VO. (b) VO with sun sensor and inclinometer.

To summarize, we have shown on a large set of individual traverses the statistical error improvement of VO with sun sensor and inclinometer measurements included. However, it is beneficial to focus on a single typical example of these traverses, in order to glean some finer detail. For this paper, we will focus on Section 14, which demonstrates a typical error improvement. To visualize how our algorithm affects the motion estimate itself, we have presented the Section 14 traverse and motion estimates in Figure 12(a). We observe that the heading error is greatly reduced, because of the corrections of the sun sensor, as well as the pitch error, because of the corrections of the inclinometer. Figure 12(a) also illustrates the growth of the 99.7% uncertainty ellipses over a number of timesteps from the traverse.

We note that the incorporation of the sun sensor and inclinometer measurements significantly reduces the uncertainty in the robot's location at any given time. This result is shown in finer detail in Figures 13 and 14, illustrating the uncertainty envelopes

for the Section 14 traverse. Once again, the significant accuracy improvements provided by the sun sensor and inclinometer are achieved with very low additional computational cost.

As a final demonstration of the benefits of continuous sun sensor and inclinometer corrections, we have computed path estimates for the full 10-km traverse. The results are presented in Figures 15 and 16, with path estimates from three different versions of our algorithm. The first is straight VO, with no additional measurements used at any point. The second variation is VO with periodic orientation updates from the sun sensor and inclinometer at the start of each new section (approximately every 500 m), as previously demonstrated by Carle, Furgale, and Barfoot (2010). These periodic updates are computed by allowing the vehicle to remain at rest for an extended period of time, in order to collect a large number of measurements. A batch solution method is then used to accurately compute the vehicle attitude, as described by Enright et al. (2009). This version of our algorithm is similar to

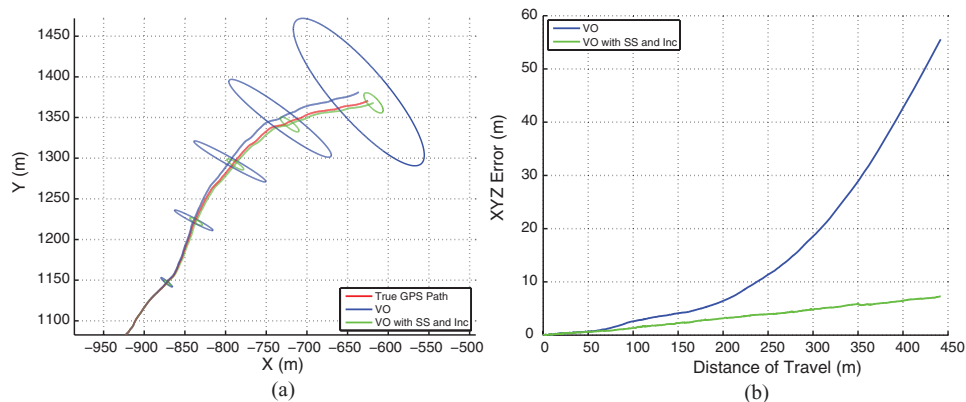


Figure 12. Estimated path results of our algorithm on Section 14 of the traverse, illustrating the accuracy improvement from using the sun sensor and inclinometer. (a) Estimated motion path for Section 14, with 99.7% uncertainty ellipses shown. (b) Error growth as a function of distance for Section 14. Note that the superlinear error growth of VO has been reduced to a more linear curve using sun sensor and inclinometer measurements.

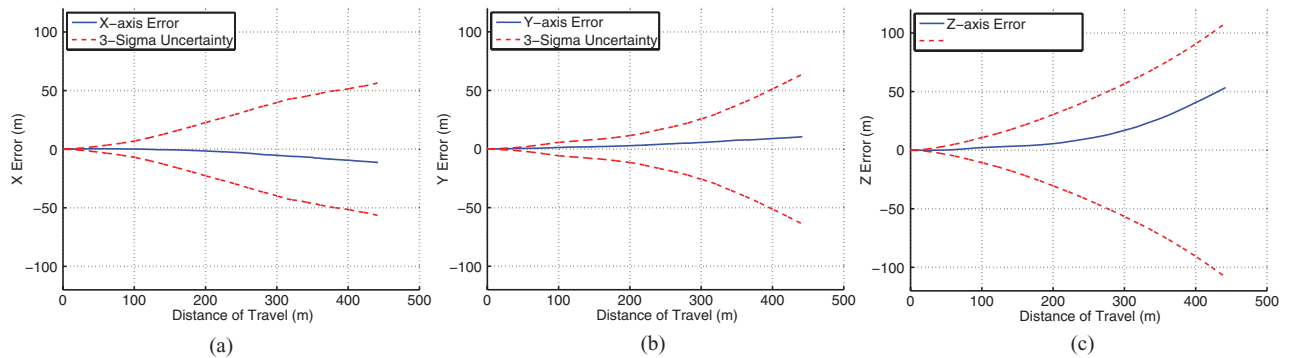


Figure 13. X- (left), Y- (middle), and Z- (right) axis error plots for the Section 14 traverse, estimated without sun sensor and inclinometer measurements.

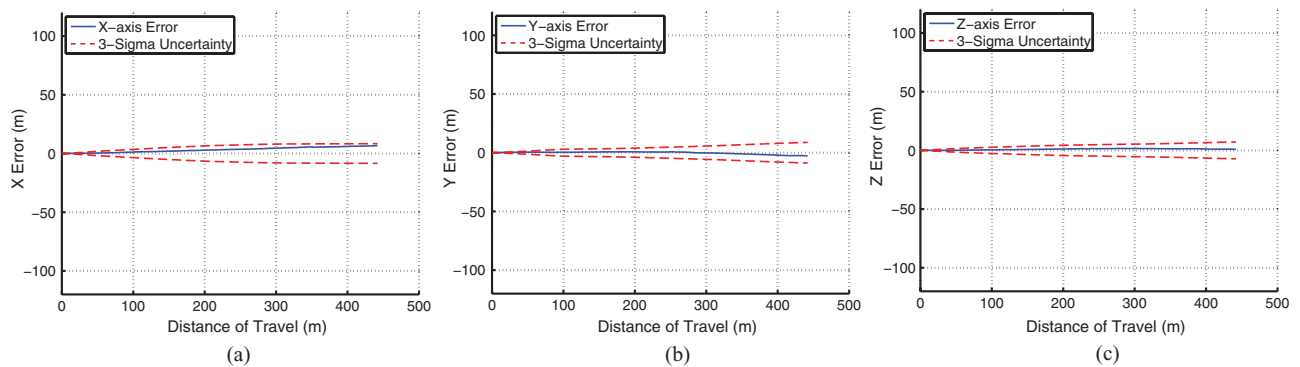


Figure 14. X- (left), Y- (middle), and Z- (right) axis error plots for the Section 14 traverse, estimated using sun sensor and inclinometer measurements.

the approach of the MERs, where sun measurements are periodically used to update the rover's orientation. The third version of our algorithm is VO with continuous corrections from the sun sensor and inclinometer, as described in Section 3. Figure 15 illustrates that continuous correction of the vehicle's orientation using sun sensor and inclinometer measurements greatly restricts the error growth, producing an error of only 0.6% at the end of the 10-km traverse. We also observe that continuous corrections are significantly more accurate than only periodically updating the attitude, with very low additional computational cost. In summary, over such a long traverse, we can significantly improve our VO system with minimal additional computation, power, or mass, simply by including a sun sensor and inclinometer. To provide more detail about the terrain along the traverse, Figure 17 has also been included, showing the GPS altitude as a function of path length. The index and starting time of each individual traverse section has also been indicated.

For this 10-km traverse, it is interesting to note that the altitude estimate is responsible for a large portion of the error. We believe that forward-facing stereo-based VO inherently tends to drift in the vertical direction for planetary applications because of the nominally oblique presentation of the terrain to the camera and the nature of the nonlinearities in a stereo rig (Sibley, Matthies, & Sukhatme, 2005). As we have observed in Figure 16(b), including

absolute attitude measurements helps to reduce this bias, as does increasing the numbers of frames over which the optimization is performed (Konolige et al., 2007). Further investigation of this bias will be the subject of future work.

5.4. Using the Sun Sensor and Inclinometer to Reduce Computation

In addition to the accuracy gains demonstrated in Section 5.3, we can also use the sun sensor and inclinometer measurements to lessen the computational requirements of VO. As previously mentioned, the use of VO on the MERs has been severely limited by slow computation time. The hardware configuration of the rovers, including a space-qualified 20-MHz processor and slow-throughput camera bus, results in each VO update cycle taking up to 3 min to compute (Maimone et al., 2007). Thus, in the interest of covering maximal ground, the use of VO has been restricted to short drives, typically less than 15 m in length. A simple approach to reducing this computational burden would be to acquire and process fewer stereo images per distance of travel. However, because of the increased spatial transformation of the camera between images, key-point tracking becomes more difficult as the frame rate is decreased. With fewer key points, we would expect a less accurate visual odometry estimate. Our

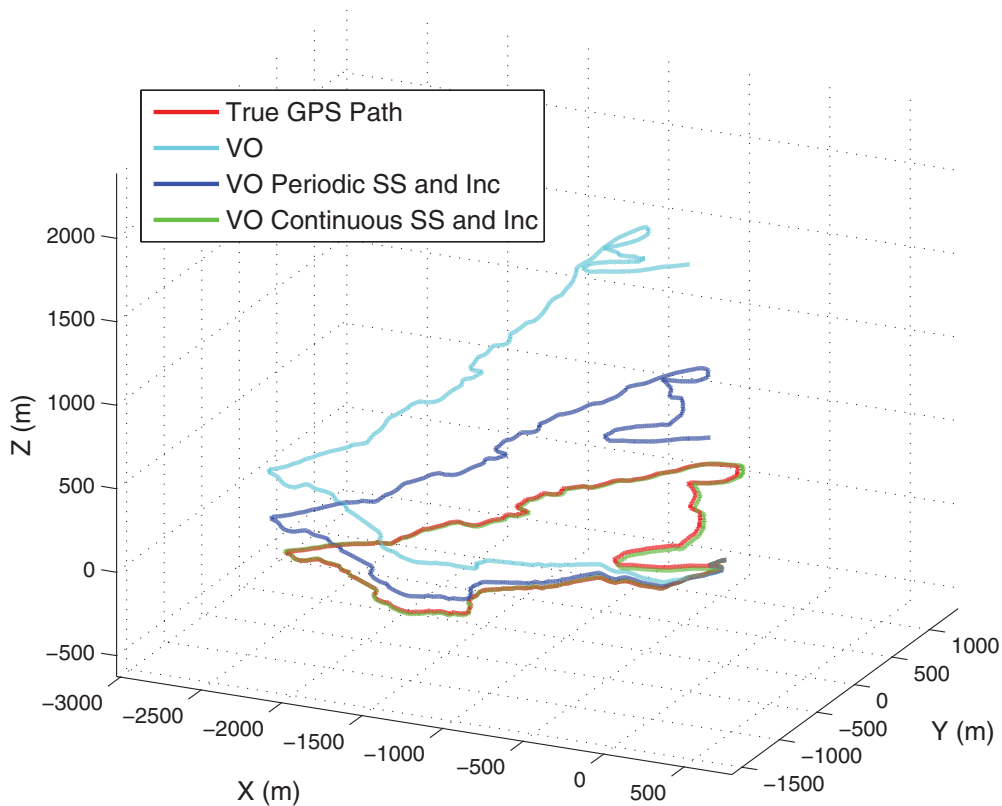


Figure 15. Three-dimensional view of motion estimate results for the full 10-km traverse.

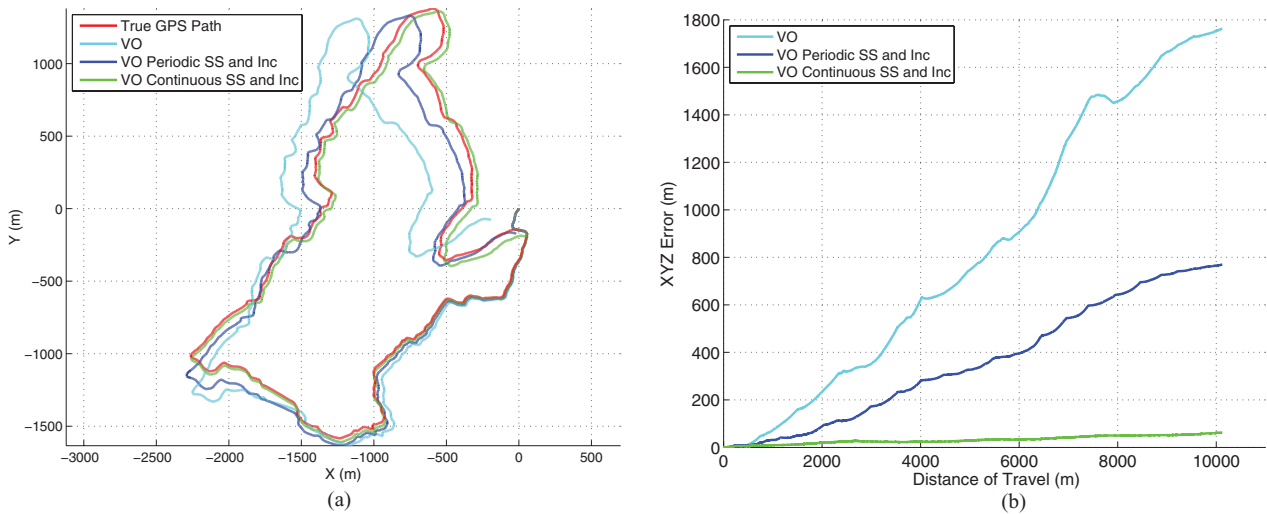


Figure 16. Additional results from the full 10-km traverse, illustrating that the continuous orientation corrections from the sun sensor and inclinometer greatly limit error growth in the VO motion estimate. (a) X–Y plane view of motion estimate results. (b) Error growth as a function of distance.

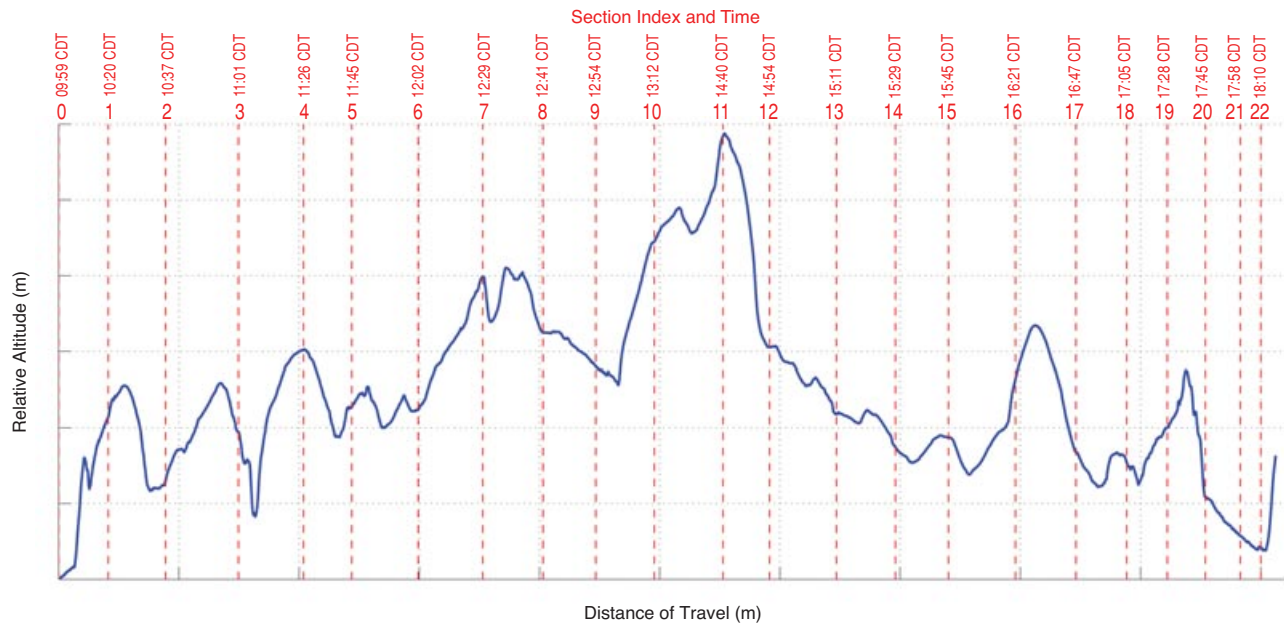


Figure 17. Altitude from GPS, relative to start of 10-km loop, as a function of distance. The individual traverse section indices have been indicated, as well as the Central Daylight Time (CDT) at the beginning of each traverse.

proposed algorithm compensates for this loss of accuracy by incorporating absolute orientation information from low-cost sun sensor and inclinometer measurements. The idea is to reduce the computational burden of VO per distance of travel, while maintaining accuracy comparable to that of conventional VO.

As a demonstration of this concept, we gradually reduced the number of images in our Devon Island data set and computed corresponding VO estimates. Note that this also led to a reduced number of sun sensor and inclinometer readings, because these measurements must be associated with stereo images acquired

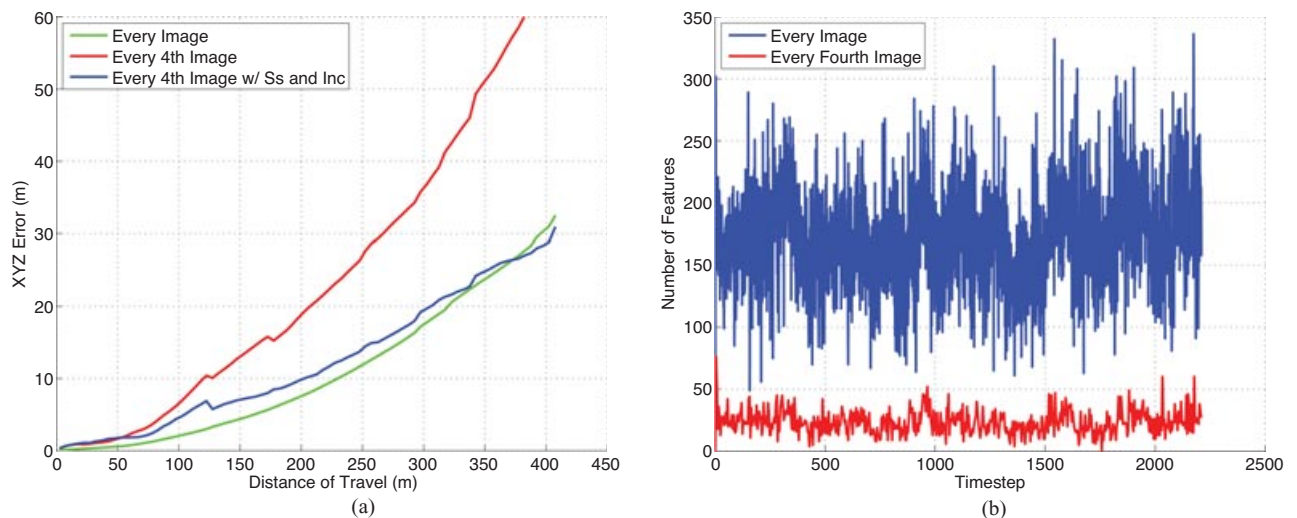


Figure 18. Results produced by processing every fourth stereo image that was acquired, to reduce the computational burden of VO. (a) Mean XYZ error curves for varying frame rates, illustrating the average error for all 23 traverse sections. Note that the low-frame-rate result with sun sensor and inclinometer measurements included closely resembles the high-frame-rate result. (b) Number of tracked keypoints for Section 14, illustrating the greatly reduced number of keypoints at low framerate.

at approximately the same time. Perhaps counterintuitively, we observed that reducing the frame rate actually initially produced less error in the motion estimate. This phenomena has been previously described by Howard (2008), who noted that higher VO frame rates will integrate more noise into the motion estimate. Although the accuracy did improve initially, further reducing the frame rate eventually resulted in sufficiently few tracked key points to produce a poor VO estimate. For our data set and algorithm, this was observed when every fourth stereo image was processed. Figure 18(b) illustrates the significantly reduced number of tracked key points at a low frame rate for the representative Section 14 traverse. We then computed new motion estimates for all 23 traverse sections incorporating sun sensor and inclinometer measurements, producing the mean error curves observed in Figure 18(a). The absolute orientation corrections bring the low frame rate errors back into a range comparable to the high frame rate results, and, quite often, are even more accurate. This comparable error comes at a greatly reduced cost, because we are computing four times fewer VO updates, processing significantly fewer key points, and the additional cost of the sun sensor and inclinometer measurements is nearly negligible.

6. CONCLUSIONS

In this paper, we have presented a novel algorithm for incorporating sun sensor and inclinometer measurements directly into the VO solution using bundle adjustment. Through rigorous testing on 10 km of data from a planetary analogue environment, we demonstrated that these absolute orientation measurements greatly restrict the error growth of the motion estimate, especially over long traversal distances. For future planetary exploration missions, long-range autonomous driving may expand the capabilities and science-gathering abilities of rovers. Although the use of a magnetic compass is not possible on the Moon or Mars, the inclusion of sun sensor and inclinometer measurements is able to keep the rover accurately on course during these traverses. Importantly, incorporating these additional measurements comes at a minimal cost in terms of power, weight, and computation. In other words, one could easily improve an existing VO system with minimal effort and cost by adding and integrating these two sensors. Looking forward, we plan to investigate methods of further improving the quality of our VO estimates. One such approach would be to use a sliding window approach for VO, including measurements from a handful of previous timesteps in the estimate. Additional field tests have been planned to investigate such improvements.

ACKNOWLEDGMENTS

The authors would like to thank Mr. Doug Sinclair of Sinclair Interplanetary for the donation of a SS-411 Digital Sun Sensor. Funding for this work was provided in part by the Natural Sciences and Engineering Research Council (NSERC) of Canada. Funding for our field trials on Devon Island was provided by the Canadian Space Agency's Canadian Analogue Research Network (CARN) program. Thanks to the Mars Institute and the

Haughton-Mars Project for providing infrastructure and logistics on Devon Island. The authors are grateful to the members of the communities of Resolute Bay, Grise Fjord, and Pond Inlet who acted as guides on Devon Island.

REFERENCES

- Barfoot, T. D., Forbes, J. R., & Furgale, P. T. (2010). Pose estimation using linearized rotations and quaternion algebra. *Acta Astronautica*, 68(1–2), 101–112.
- Bay, H., Ess, A., Tuytelaars, T., & Gool, L. V. (2008). Speeded-up robust features (SURF). *Computer Vision and Image Understanding*, 110(3), 346–359.
- Brown, D. C. (1958). A solution to the general problem of multiple station analytical stereotriangulation. (RCP-MTP Data Reduction Tech. Rep. 43). Patrick Air Force Base, Cocoa Beach, FL. (Also designated as AFMTC 58-8)
- Carle, P., Furgale, P. T., & Barfoot, T. D. (2010). Long-range rover localization by matching Lidar scans to orbital elevation maps. *Journal of Field Robotics*, 27(3), 344–370.
- Eisenman, A., Liebe, C., & Perez, R. (2002, March). Sun sensing on the Mars exploration rovers. In *Proceedings of the IEEE Aerospace Conference*, Big Sky, MT.
- Enright, J., Furgale, P., & Barfoot, T. D. (2009, March). Sun sensing for planetary rover navigation. In *Proceedings of the IEEE Aerospace Conference*, Big Sky, MT.
- Enright, J., & Sinclair, D. (2007, August). Algorithm enhancements for the SS-411 digital sun sensor. In *Proceedings of the 21st Annual AIAA/USU Conference on Small Satellites*, Logan, UT.
- Furgale, P. T., & Barfoot, T. D. (2010). Visual teach and repeat for long-range rover autonomy. Special issue on “Visual mapping and navigation outdoors,” *Journal of Field Robotics*, 27(5), 534–560.
- Furgale, P. T., Carle, P., Enright, J., & Barfoot, T. D. (2012). The Devon Island Rover Navigation Dataset. *International Journal of Robotics Research* (in press).
- Furgale, P., Enright, J., & Barfoot, T. (2011). Sun sensor navigation for planetary rovers: Theory and field testing. *IEEE Transactions on Aerospace and Electronic Systems*, 47(3), 1631–1647.
- Harris, C., & Stephens, M. (1988, August). A combined corner and edge detection. In *Proceedings of the Fourth Alvey Vision Conference*, Manchester, England (pp. 147–151).
- Howard, A. (2008, September). Real-time stereo visual odometry for autonomous ground vehicles. In *Proceedings of the IEEE/RSJ International Conference on Intelligent Robots and Systems (IROS 2008)*, Nice, France.
- Hughes, P. C. (1986). *Spacecraft attitude dynamics*. New York: John Wiley & Sons.
- Konolige, K., Agrawal, M., & Solà, J. (2007, November). Large scale visual odometry for rough terrain. In *Proceedings of the International Symposium on Research in Robotics (ISRR)*, Hiroshima, Japan.
- Lambert, A., Furgale, P., Barfoot, T. D., & Enright, J. (2011, March). Visual odometry aided by a sun sensor and inclinometer. In *Proceedings of the IEEE Aerospace Conference*, Big Sky, MT.
- Lee, P., Bunch, T. E., Cabrol, N., Cockell, C. S., Grieve, R. A. F., Rice, J. W., McKay, C. P., Chutt, J. W., & Zent, A. P. (1998, March).

- Haughton-Mars 97: I. Overview of observations at the Haughton Impact Crater, a unique Mars analog site in the Canadian high Arctic. In Proceedings of the 29th Lunar and Planetary Science Conference, Houston, TX.
- Maimone, M., Cheng, Y., & Matthies, L. (2007). Two years of visual odometry on the Mars exploration rovers. *Journal of Field Robotics*, 24(3), 169–186.
- Matthies, L. (1992). Stereo vision for planetary rovers—stochastic modeling to near real-time implementation. *International Journal of Computer Vision*, 8(1), 71–91.
- Matthies, L., Maimone, M., Johnson, A., Cheng, Y., Willson, R., Villalpando, C., Goldberg, S., Huertas, A., Stein, A., & Angelova, A. (2007). Computer vision on Mars. *International Journal of Computer Vision*, 75(1), 67–92.
- Matthies, L., & Shafer, S. (1987). Error modeling in stereo navigation. *IEEE Journal of Robotics and Automation*, RA-3(1), 239–250.
- Mei, C., Sibley, G., Cummins, M., Newman, P., & Reid, I. (2011). RSLAM: A system for large-scale mapping in constant-time using stereo. *International Journal of Computer Vision*, 94(2), 198–214.
- Moravec, H. (1980). Obstacle avoidance and navigation in the real world by a seeing robot rover (Tech. Rep. CMU-RI-TR-80-03). Pittsburgh, PA: Robotics Institute, Carnegie Mellon University.
- Nister, D., Naroditsky, O., & Bergen, J. (2006). Visual odometry for ground vehicle applications. *Journal of Field Robotics*, 23(1), 3–20.
- Olson, C. F., Matthies, L. H., Schoppers, M., & Maimone, M. W. (2003). Rover navigation using stereo ego-motion. *Robotics and Autonomous Systems*, 43(4), 215–229.
- Rosten, E., & Drummond, T. (2005, October). Fusing points and lines for high performance tracking. In Proceedings of the IEEE International Conference on Computer Vision, Beijing, China.
- Rosten, E., & Drummond, T. (2006, May). Machine learning for high-speed corner detection. In Proceedings of the European Conference on Computer Vision, Graz, Austria.
- Sibley, G., Matthies, L., & Sukhatme, G. (2005, October). Bias reduction filter convergence for long range stereo. In Results of the 12th International Symposium of Robotics Research, San Francisco, CA.
- Sibley, G., Mei, C., Reid, I., & Newman, P. (2010). Vast-scale outdoor navigation using adaptive relative bundle adjustment. *International Journal of Robotics Research*, 29(8), 958–980.
- Trebi-Ollennu, A., Huntsberger, T., Cheng, Y., Baumgartner, E., Kennedy, B., & Schenker, P. (2001). Design and analysis of a sun sensor for planetary rover absolute heading detection. *IEEE Transactions on Robotics and Automation*, 17(6), 939–947.
- Volpe, R. (1999, October). Mars rover navigation results using sun sensor heading determination. In Proceedings of the IEEE/RSJ International Conference on Intelligent Robots and Systems (IROS 1999), Kyongju, Korea.
- Wilcox, B., & Nguyen, T. (1998, July). Sojourner on Mars and lessons learned for future planetary rovers. In Proceedings of the 28th SAE International Conference on Environmental Systems (ICES), Danvers, MA.